

# Multi-scale snowdrift-permitting modelling of mountain snowpack

Vincent Vionnet<sup>1,2</sup>, Christopher B. Marsh<sup>1</sup>, Brian Menounos<sup>3</sup>, Simon Gascoïn<sup>4</sup>, Nicholas E. Wayand<sup>1</sup>, Joseph Shea<sup>3</sup>, Kriti Mukherjee<sup>3</sup> and John W. Pomeroy<sup>1</sup>.

5 <sup>1</sup>Centre for Hydrology, University of Saskatchewan, Saskatoon, Canada

<sup>2</sup>Environmental Numerical Prediction Research, Environment and Climate Change Canada, Dorval, QC, Canada

<sup>3</sup>Natural Resources and Environmental Studies Institute and Geography Program, University of Northern British Columbia, Prince George, V2N 4Z9, Canada

<sup>4</sup>Centre d'Études Spatiales de la Biosphère, UPS/CNRS/IRD/INRAE/CNES, Toulouse, France

10

*Correspondence to:* Vincent Vionnet (vincent.vionnet@canada.ca)

**Abstract.** The interaction of mountain terrain with meteorological processes causes substantial temporal and spatial variability in snow accumulation and ablation. Processes impacted by complex terrain include large-scale orographic enhancement of snowfall, small-scale processes such as gravitational and wind-induced transport of snow, and variability in the radiative balance such as through terrain shadowing. In this study, a multi-scale modeling approach is proposed to simulate the temporal and spatial evolution of high mountain snowpacks. The multi-scale approach combines atmospheric data from a numerical weather prediction system at km-scale with process-based downscaling techniques to drive the Canadian Hydrological Model (CHM) at spatial resolutions allowing for explicit snow redistribution modelling. CHM permits a variable spatial resolution by using the efficient terrain representation by unstructured triangular meshes. The model simulates processes such as radiation shadowing and irradiance to slopes, blowing snow transport (saltation and suspension) and sublimation, avalanching, forest canopy interception and sublimation and snowpack melt. Short-term, km-scale atmospheric forecasts from Environment and Climate Change Canada's Global Environmental Multiscale Model through its High Resolution Deterministic Prediction System (HRDPS) drive CHM, and are downscaled to the unstructured mesh scale. In particular, a new wind downscaling strategy uses pre-computed wind fields from a mass-conserving wind model at 50-m resolution to perturb the meso-scale HRDPS wind and to account for the influence of topographic features on wind direction and speed. HRDPS-CHM was applied to simulate snow conditions down to 50-m resolution during winter 2017/2018 in a domain around the Kananaskis Valley (~1000 km<sup>2</sup>) in the Canadian Rockies. Simulations were evaluated using high-resolution airborne Light Detection and Ranging (LiDAR) snow depth data and snow persistence indexes derived from remotely sensed imagery. Results included model falsifications and showed that both wind-induced and gravitational snow redistribution need to be simulated to capture the snowpack variability and the evolution of snow depth and persistence with elevation across the region. Accumulation of wind-blown snow on leeward slopes and associated snow-cover persistence were underestimated in a CHM simulation driven by wind fields that did not capture leeside flow recirculation and associated wind speed decreases. A terrain-based metric helped to identify these lee-side areas and improved the wind field and the associated snow redistribution. An overestimation of snow

15  
20  
25  
30

redistribution from windward to leeward slopes and subsequent avalanching was still found. The results of this study highlight  
35 the need for further improvements of snowdrift-permitting models for large-scale applications, in particular the representation  
of subgrid topographic effects on snow transport.

## 1 Introduction

High mountain snowpacks are characterized by a strong spatial and temporal variability that is associated with elevation,  
vegetation cover, slope steepness, orientation and wind exposure. This variability results from processes occurring during the  
40 snow accumulation and ablation periods at a large range of spatial scales (e.g., Pomeroy and Gray, 1995; Pomeroy et al., 1998;  
2012; 2016; Clark et al., 2011; Mott et al., 2018). Snow accumulation at the mountain range scale (1-500 km) is primarily  
dominated by orographic precipitation, and results in regions of enhanced or reduced snowfall (e.g., Houze, 2012). At the  
mountain-ridge and slope scales (5 m – 1 km), preferential deposition of snowfall and blowing snow transport, including  
transport in both saltation and suspension layers, strongly impact snow accumulation (e.g., Mott et al. 2018). Redistribution  
45 by avalanches (e.g., Bernhardt and Schulz, 2010; Sommer et al., 2015) and surface and blowing snow sublimation (e.g.,  
MacDonald et al., 2010; Vionnet et al., 2014; Musselman et al., 2015; Sextone et al., 2018) also modify the spatial variability  
of snow. During the ablation period, spatially varying melt rates result from differences in solar irradiance due to aspect and  
shading (e.g., Marks and Dozier, 1992; Marsh et al., 2012), in net solar irradiance due to albedo variations (e.g., Dumont et  
al., 2011; Schirmer and Pomeroy, 2020), in turbulent fluxes (e.g., Winstral and Marks, 2014; Gravelman et al., 2015) and in  
50 advected heat from snow-free ground in patchy snow cover conditions (e.g., Mott et al., 2013; Harder et al., 2017; Schögl et  
al., 2018).

The multi-scale variability of mountain snow represents a challenge for snow models used in support of avalanche hazard  
forecasting (Morin et al., 2020), hydrological predictions (e.g., Warscher et al., 2013; Brauchli et al., 2017; Freudiger et al.,  
2017) and climate projections (e.g., Rasouli et al., 2014; Hanzer et al., 2018) in mountainous terrain. Several modelling  
55 strategies have been proposed to face this challenge and to capture this multi-scale variability. At the mountain range scale,  
atmospheric models at sufficient resolutions (4-km or finer) can bring valuable information on the variability of snowfall and  
resulting snow accumulation (e.g., Prein et al., 2015; Lundquist et al., 2019; Fang and Pomeroy, 2020). Indeed, at these  
resolutions, atmospheric models operate at convection-permitting scales, and explicitly represent convection and highly  
resolved vertical motions, achieving improved estimates of snowfall (e.g., Rasmussen et al., 2011). Sub-grid parameterizations  
60 of snow depth have been proposed to represent the snow variability at the mountain-ridge and slope-scale for snowpack models  
operating at km scales (Liston, 2004; Helbig and van Herwijnen, 2017; He and Ohara, 2019). Another strategy consists of  
explicitly modelling the snow evolution at the mountain-ridges and slopes scales at resolutions ranging from a few meters to  
200 meters (Liston, 2004; Musselman et al., 2015). At these scales, the variability of snow accumulation can be represented  
using (i) simple parameterizations to adjust snowfall as a function of topographic parameters (e.g., Winstral and Marks, 2002;  
65 Hanzer et al., 2016) or (ii) using models that explicitly represent preferential deposition and/or wind-induced snow

redistribution (e.g., Essery et al., 1999; Durand et al., 2005; Pomeroy et al., 2007; Liston et al., 2007; Lehning et al., 2008; Sauter et al., 2013; Vionnet et al., 2014; Marsh et al., 2020a). These models can be classified as snowdrift-permitting models since they operate at sufficient resolutions (200-m or finer) to activate the horizontal redistribution of snow between computational elements. High resolution remote sensing data assimilation can also be used at these scales to correct spatial  
70 biases in the atmospheric forcing and to account for missing physical processes in the models (e.g., Durand et al., 2008; Baba et al., 2018).

Snowdrift-permitting models simulate wind-induced snow transport in the saltation and suspension layers (e.g, Pomeroy and Gray, 1995). As proposed by Mott et al. (2018), they can be divided into two main categories: (i) models solving the vertically-integrated mass flux in the saltation and suspension layers (Essery et al., 1999; Durand et al., 2005; Pomeroy et al., 2007; Liston et al., 2007) and (ii) models solving the three-dimensional (3-D) advection-turbulent diffusion equation of blown snow  
75 particles in the atmosphere (Gauer, 1998; Lehning et al., 2008; Schneiderbauer and Prokop, 2011; Sauter et al., 2013; Vionnet et al., 2014). One of the main challenges for all these models is obtaining accurate driving wind fields at sufficient high resolution since they strongly impact the accuracy of simulated snow redistribution (Mott and Lehning, 2010; Musselman et al., 2015). Models of the first category need two-dimensional (2-D) driving wind fields. Liston et al. (2007), inspired by Ryan  
80 (1977), proposed the use of terrain-based parameters to adjust distributed wind fields to the local topography. These distributed wind fields can be obtained from interpolated station data (Gascoïn et al., 2013; Sextone et al., 2018), hourly output from regional climate model at convective-permitting scale (Reveillet et al., 2020), or a pre-computed wind field library using an atmospheric model (Berhnhardt et al., 2010). Essery et al. (1999) used a linearized turbulence model (Walmsley et al., 1982) to build a pre-computed library of 2-D wind maps to distribute wind measurements from stations data. Musselman et al. (2015)  
85 showed that this approach led to more accurate simulations of snow redistribution around an alpine crest than wind fields derived from the terrain-based parameters proposed by Liston et al. (2007). Models of the second category require a 3-D representation of the wind field and associated atmospheric turbulence. In this case, driving wind fields can be obtained from computational fluid dynamics (CFD) models (Gauer, 1998; Schneiderbauer and Prokop, 2011), or atmospheric models in Large Eddy Simulations (LES) mode used to generate library of pre-computed wind fields (Lehning et al., 2008; Mott and  
90 Lehning, 2010) or fully coupled to a snowpack model (Vionnet et al., 2014). These advanced models can be used for detailed studies such as the feedbacks between blowing snow sublimation and the atmosphere (Groot Zwaafink et al., 2011) or the processes driving the variability of snow accumulation during a snowfall event, including preferential deposition of snowfall (Lehning et al., 2008; Mott et al., 2010; Vionnet et al., 2017).

Differences in the level of complexity of snowdrift-permitting models and associated driving wind fields influence the spatial  
95 and temporal ranges of application of these models. Due to their relatively low computational costs, models of the first category can be applied to simulate the snow cover evolution over entire snow seasons at resolution between 25 and 200 m for regions covering hundreds of km<sup>2</sup> (e.g., 210 km<sup>2</sup> for Berhnhardt et al. (2010); 1043 km<sup>2</sup> for Gascoïn et al. (2013); 3600 km<sup>2</sup> for Sextone et al. (2018)). On the other hand, models of the second category are usually restricted to the simulation of single blowing snow events at resolution between 2 m and 50 m over regions covering tens of km<sup>2</sup> (e.g., 1 km<sup>2</sup> in Schneiderbauer and Prokop (2011),

100 2.3 km<sup>2</sup> in Mott and Lehning (2010); 23 km<sup>2</sup> in Vionnet et al. (2017)). The study by Groot Zwaafink et al. (2013) is an exception and relied on the Alpine 3D model (Lehning et al., 2008) to simulate the snow cover evolution at 10-m resolution over a region of 2.4 km<sup>2</sup> of the Swiss Alps for an entire winter. All these snowdrift-permitting models used a gridded representation of the topography. Large-scale applications of these models over mountainous area are limited by the need to have a fixed and sufficiently high resolution over large areas even in regions where wind-induced snow transport is not active  
105 (valley bottom for example).

To overcome some of these limitations, Marsh et al. (2020a) developed a snowdrift-permitting scheme of intermediate complexity that solves the 3-D advection-diffusion blowing snow transport on a variable resolution unstructured mesh. This scheme is implemented in the Canadian Hydrological Model (CHM; Marsh et al., 2020b). The landscape is discretized using a variable resolution unstructured mesh that allows an accurate representation of terrain heterogeneities with limited  
110 computation elements (Marsh et al., 2018). Marsh et al. (2020a) used the WindNinja diagnostic wind model (Forthofer et al., 2014) to build libraries of pre-computed wind fields. Wagenbrenner et al. (2016) showed that WindNinja can be used to downscale wind field from atmospheric models running at convection-permitting scale in complex terrain.

The objective of this study is to present and evaluate a novel strategy for multi-scale modelling of mountain snowpack over large regions and for entire snow seasons. Specifically: (1) Can efficient wind-downscaling approaches be used for blowing  
115 simulation? (2) Over large spatial extents, can lateral mass redistribution (blowing snow and avalanching) be ignored? (3) Can optical satellite imagery be used to diagnose model performances over large spatial extents? This modelling strategy combines (i) atmospheric forcing from the convection-permitting Canadian Numerical Weather Prediction (NWP) system, (ii) a downscaling module including wind fields from a high-resolution diagnostic wind model and (iii) the multi-scale snowdrift-permitting model CHM running on an unstructured mesh. This modelling strategy was applied for a full winter over a domain  
120 of 958 km<sup>2</sup> around the Kananaskis Valley in the Canadian Rockies. Different model configurations were tested to assess the impact of the representation of physical processes in CHM as well as the complexity of the wind downscaling scheme. Airborne LiDAR snow depth data and snow persistence indexes derived from Sentinel-2 images were used to evaluate the ability of the different CHM configurations to capture the elevation-snow depth relationship as well as snow redistribution around wind-exposed ridges. The paper is organized as follows: Section 2 presents the study area and the different observation datasets used  
125 in this study, and also describes the CHM modelling platform, the wind downscaling strategy and the configurations of the CHM experiments; Section 3 evaluates the impact of the wind field downscaling and the quality of the snowpack simulations using airborne LiDAR snow depth data and snow persistence indexes; Section 4 discusses the main challenges associated with snowdrift-permitting modelling of mountain snowpack and associated limitations. Finally, concluding remarks are presented in Section 5.

**2.1 Study Site**

This work studies the evolution of the mountain snowpack around the Kananaskis Valley of the Canadian Rockies, Alberta (Fig. 1). The study domain covers an area of 958 km<sup>2</sup> and is characterized by a complex and rugged topography with elevations ranging from 1400 m a.s.l. at the Kananaskis valley bottom in the northeastern part of the domain up to 3406 m a.s.l. at the summit of Mount Sir Douglas in the southern part of the region (Fig. 1b). Valley bottoms and lower slopes are predominately covered by needleleaf evergreen forest (Fig. 1a). Short shrubs and low vegetation are present near treeline whereas exposed rock surfaces, talus and grasses are found in the highest alpine elevations. The Kananaskis Valley hosts several meteorological stations that are part of the University of Saskatchewan's Canadian Rockies Hydrological Observatory (CRHO; <https://research-groups.usask.ca/hydrology/science/research-facilities/crho.php>) and is active for research in snow hydrology (e.g., MacDonald et al., 2010; Musselman et al., 2015; Pomeroy et al., 2012; 2016; Fang et al., 2019; Fang and Pomeroy, 2020). More details about these meteorological stations are given in Sect. 2.3.1.

**2.2 Model****2.2.1 Mesh generation**

The Digital Elevation Model (DEM) from the Shuttle Radar Topography Mission-SRTM (EROS Center, 2017) at a resolution of 1-arc second (30 m) was used as input to the *mesher* code (Marsh et al., 2018) to generate an unstructured, variable resolution triangular mesh over the Kananaskis domain (Fig. 1). In *mesher*, triangles are bounded with minimum and maximum areas and are generated to fulfil a given tolerance defined here as the root mean square error to the underlying topographic raster. This study uses a high-resolution mesh, denoted  $M^{l^5}_{50}$ , with a minimum triangle area of 50 m × 50 m and a vertical tolerance of 15 m. The characteristics of the generated mesh are given in Table 1. For the Kananaskis domain, 383 200 raster grid cells with a 50 m resolution are required to represent the terrain, whereas 101 700 triangles are used in  $M^{l^5}_{50}$  (Fig. 2). Large triangles are found in valley bottoms of low topographic variability, whereas small triangles dominate in alpine terrain, close to ridges where wind-induced snow redistribution is common.

A dataset of tall vegetation (>5 m) coverage, with a resolution of 30 m (Fig. 1a), was obtained from Hansen et al. (2013). These fractional values were applied to the triangular mesh via *mesher* by averaging the raster cells that correspond to each triangle and assigning this average to the triangle. Triangles with an average fraction of high-vegetation larger than 0.5 were classified as forest.

**2.2.2 Snowpack model**

Distributed snowpack simulations over the triangular mesh of the study area were performed using the version of the Snobal scheme (Marks et al. 1999) implemented in CHM (Marsh et al. 2020b). Snobal has been used in numerous mountainous regions

160 across North America (e.g., Garen and Marks, 2005; Pomeroy et al., 2016; Hedrick et al., 2018). Snobal is a physically based snowpack model that approximates the snowpack with two layers. The surface layer was implemented here with a fixed thickness of 0.1 m and is used to estimate surface temperature for outgoing longwave radiation and turbulent heat fluxes. The second lower layer represents the remaining snowpack. For each layer, Snobal simulates the evolution of the snow water equivalent (SWE), temperature, density, cold content, and liquid water content. The version of Snobal used in this study  
165 includes an improved algorithm for snow compaction that accounts for bulk compaction and temperature metamorphism (Hedrick et al., 2018). Snobal in CHM employs the snow albedo routine of Verseghy et al. (1993). The ground heat flux assumes heat flow to a single soil layer of known temperature and thermal conductivity. In these simulations, the soil temperature was set to  $-4^{\circ}\text{C}$  at 10 cm below the soil-snow interface. Marsh et al. (2020b) used the same value for Snobal simulations with CHM at the Marmot Creek Research Basin located further north in the Kananaskis Valley (Fig. 1).

170 CHM also includes a 3-D advection-diffusion blowing snow transport and sublimation model (Marsh et al., 2020a): the 3-D Prairie Blowing Snow Model (PBSM-3D). This scheme uses a finite volume method discretization on the unstructured mesh. It deploys the parameterization of Li and Pomeroy (1997) to determine the threshold wind speed for snow transport initiation as a function of air temperature and snow presence. It does not depend on the properties of surface snow (e.g. density, liquid water content) simulated by Snobal (see Sect 4.4 for a discussion on the limitation of this approach). In case of blowing snow  
175 occurrence, the steady-state saltation parameterization of Pomeroy et al. (1990) is used to compute the mass concentration in the saltation layer. The concentration in the saltation layer is impacted by shear stress partitioning due to the presence of vegetation (such as shrubs) and the upwind fetch. Upwind fetch is calculated for each triangle of the mesh using the *fetchr* parameterization of Lapen and Martz (1993) and is used to reduce the mass concentration in the saltation layer in regions where flow is developing. The saltation layer acts as a lower boundary condition for the suspension layer, which is discretized  
180 with a user-defined number of layers to resolve the gradient of concentration of blowing snow particles in the suspension layer. For each layer, PBSM-3D solves the evolution of the concentration of blowing snow particles accounting for advection, turbulent diffusion, sedimentation and mass loss due to sublimation based on the parameterizations proposed by Pomeroy and Male (1992) and Pomeroy et al. (1993). At a given time step, erosion and deposition rates are computed as the spatial divergence of the saltation and suspension fluxes and the snowpack simulated by Snobal is updated accordingly. In this study,  
185 10 layers were used for a total height of the suspension layer of 5 m as in Marsh et al. (2020a). Snowfall over complex terrain is calculated by GEM according to its microphysics scheme (Milbrandt et al., 2016). CHM does not simulate explicitly preferential deposition of snowfall (Lehning et al., 2008; Mott et al., 2018). New snow is added to the surface layer in Snobal and, if wind speeds exceed the threshold wind speed, it is transported in the saltation and suspension blowing snow layers by PBSM-3D.

190 In steep alpine terrain, gravitational snow transport strongly affects the spatial variability of the snowpack (e.g. Sommer et al., 2015), the mass balance of glaciers (Mott et al., 2019) and modifies the runoff behaviour of alpine basins (Warscher et al. 2013). For these reasons, the SnowSlide scheme (Bernhard and Schulz, 2010) was implemented in CHM. SnowSlide is a simple topographically driven model that simulates the effects of gravitational snow transport. SnowSlide uses a snow holding

depth that decreases exponentially with increasing slope angle, limiting snow accumulation in steep terrain. SnowSlide was initially developed for regular gridded rasters and has been adapted here to the unstructured triangular mesh used by CHM. SnowSlide operates from the highest triangle of the mesh to the lowest one. If the snow depth exceeds the snow holding capacity for a given triangle, excess snow is redistributed to the lower adjacent triangles, proportionally to the elevation difference between the neighboring triangles and the original one. SnowSlide uses the total elevation (snow depth plus surface elevation) to operate. In this study, the default formulation of the snow holding depth proposed by Bernhardt and Schulz (2010) is used which leads to a maximal snow thickness (taken perpendicular to the slope) of 3.08 m, 1.11 m, 0.45 m, and 0.15 m for slopes of 30°, 45°, 60°, and 75°, respectively.

The impact of the presence of forest vegetation on snow interception, sublimation, snowpack accumulation and melt energetics are represented in CHM using the same canopy module as in the Cold Region Hydrological Model (CRHM; Ellis et al., 2010; Pomeroy et al. 2012). This module used Leaf Area Index and canopy closure to compute the effect of forests on shortwave and longwave irradiance at the snow surface. Snow interception and sublimation of intercepted snow are also represented following Hedstrom and Pomeroy (1998). In this study, the canopy module was activated for the triangles covered by forest as described in Sect. 2.2.1.

### 2.2.3 Atmospheric forcing

Snobal and PBSM-3D require the following atmospheric forcing: air temperature, humidity, wind speed, wind direction, liquid and solid precipitation rates, and longwave and shortwave irradiance. Due to the scarcity of the network of meteorological stations in the region (Fig. 1), hourly atmospheric forcings were obtained from the High-Resolution Deterministic System (HRDPS; Milbrandt et al., 2016). HRDPS is the high-resolution NWP system running the Global Environmental Multiscale Model (GEM) operationally over Canada at 2.5-km grid spacing. Successive HRDPS forecasts from the 00 and 12 UTC analysis time at 6 to 17 h lead time were extracted over the region and combined together to generate a continuous atmospheric forcing. Previous studies have also used distributed forcing data from NWP systems to drive snowpack models in mountainous terrain since these data can often represent the complex interactions between topography and atmospheric flow better than sparse meteorological measurements (Quéno et al., 2016; Vionnet et al., 2016; Havens et al. 2019; Lundquist et al., 2019; Fang and Pomeroy, 2020).

The HRDPS atmospheric forcing at 2.5-km grid spacing was downscaled to the triangles of the CHM mesh. Horizontal interpolation was first applied using inverse-distance weighting from the closest four HRDPS grid points. Corrections for elevation differences were then applied to adapt the HRDPS meteorological forcing to the high-resolution topography of the CHM mesh. Constant monthly lapse rates were used to adjust HRDPS 2-m air temperature and humidity (Kunkel, 1989; Shea et al., 2004). HRDPS temperature was reduced (increased) if the elevation of the triangle is higher (lower) than the elevation of the HRDPS grids points. Precipitation amounts were not modified to account for elevation difference as it was assumed that HRDPS already captures the main orographic effects affecting mountain precipitation (Lundquist et al., 2019). The precipitation adjustment function of Liston and Elder (2006) has been tested but it led to strong overestimation of snow depth

at high elevation (not shown), suggesting that this factor may not be adapted to account for the subgrid variability of precipitation amount within a 2.5 km grid. A cosine-correction was then applied to adjust precipitation falling on inclined triangle for mass-conservation purpose (Kienzle, 2011). Downscaled temperature and humidity were finally used to compute the precipitation phase with the psychrometric energy balance method of Harder and Pomeroy (2013) that performed well in the Kananaskis Valley. Direct and diffuse solar irradiance were taken from the HRDPS forecast and direct irradiance was corrected for slope and aspect as described in Marsh et al. (2012). Local terrain shadowing and its impact on shortwave irradiance were calculated using the algorithm of Dozier and Frew (1990) adapted for unstructured meshes as described in Marsh et al. (2020b). Longwave irradiance was adjusted for elevation difference using the climatological lapse rate of Marty et al. (2002). Finally, wind speed and direction were taken from the lowest HRDPS prognostic level at 40 m above the surface and were downscaled to the CHM mesh using the strategy described in the next section.

#### 2.2.4 Wind field downscaling

Mountain wind fields are notoriously difficult to observe and model (Davies et al., 1995), and obtaining high-resolution wind fields constitutes one of the greatest challenges for blowing snow models in mountainous terrain (e.g., Mott and Lehning, 2010; Vionnet et al., 2014; Musselman et al., 2015, Réveillet et al., 2020). In the context of this study, hourly HRDPS near-surface wind fields at the 2.5 km scale were downscaled to the CHM mesh over the full duration of the simulations (one water year). This required a computationally efficient wind downscaling method. Therefore, the wind downscaling strategy used in this study was derived from the method proposed by Barcons et al. (2018) for mesoscale-to-microscale downscaling of near-surface wind fields. This method combines precomputed microscale simulations with a mesoscale forecast using transfer functions. In their study, Barcons et al. (2018) combined the Weather Research and Forecast mesoscale model at 3-km grid spacing and the Alya-CFDWind microscale model at 40-m grid spacing. In our study, microscale wind simulations were generated with the WindNinja model. WindNinja is a mass-conserving diagnostic wind model, primarily designed to simulate mechanical effects of terrain on the flow (Forthofer et al., 2014). Forthofer et al., (2014) showed that the model captures important terrain-induced flow features, such as ridgetop acceleration or terrain channeling and can improve wildfire spread predictions in complex terrain. Wagenbrenner et al. (2016) used the model to directly downscale near-surface wind forecast from NWP systems in complex terrain.

The application and extension of the Barcons et al (2018) approach for use on an unstructured mesh and to account for direction perturbations is detailed below. First, to build the windmap library, WindNinja was run at 50-m resolution over the Kananaskis domain (Fig. 1). As WindNinja uses a regular grid, the input topography was taken from the same SRTM DEM at 30-m grid spacing that was used to build the CHM mesh (Sect. 2.2.1). WindNinja used a spatially constant roughness length ( $z_0 = 0.01$  m) representative of snow-covered terrain in alpine topography (Mott et al., 2010; Mott and Lehning, 2010) and vegetation effects were introduced later in the downscaling procedure, as described below. WindNinja simulations were carried out for 24 initial wind directions (each  $15^\circ$ ) with an initial wind speed at 40 m above the surface set to  $10 \text{ m s}^{-1}$ . The height of 40 m corresponds to the lowest HRDPS prognostic level.



260 Then, for each wind direction in the windmap library, the transfer function  $f$  was computed for use in the downscaling procedure given as:

$$f = \frac{U_{WN}}{\langle U_{WN} \rangle_L} \quad (1)$$

where  $U_{WN}$  is the local wind speed ( $U_{WN} = \sqrt{u_{WN}^2 + v_{WN}^2}$ ),  $u_{WN}$  and  $v_{WN}$  are the horizontal components of the wind at 50-m resolution, and  $\langle U_{WN} \rangle_L$  is the spatial average of  $U_{WN}$  over an area of size  $L \times L$ . By construction, when  $L$  tends towards 0,  $f$  tends towards 1. As  $L$  increases,  $f$  incorporates the local wind fluctuation induced by the micro-scale terrain features (Barcons et al., 2018). A value of  $L = 1000$  m was used in this study in agreement with the finding of Barcons et al. (2018) in complex terrain. Note that Barcons et al. (2018) used a circle instead of a square to compute the spatial average of the wind speed. Thus,  $f$  acts as a speedup/slowdown factor that accounts for topographic impacts on wind speed. Only one value for the initial wind speed was used to build the wind library due to the insensitivity of the transfer function to the initial wind speed found with WindNinja.

270 To account for impacts on direction, the following approach was taken. The rasters of the windmap library containing the horizontal  $u$  and  $v$  wind components and the transfer function  $f$  for each initial wind direction were applied to the triangles of the unstructured mesh using the *mesher* code (Marsh et al., 2018). At each CHM time step, the HRDPS  $u_{HRDPS}$  and  $v_{HRDPS}$  wind components were spatially interpolated to the triangles centres with an inverse-distance interpolant using the four closest HRDPS grid points. For each triangle, the interpolated HRDPS wind direction,  $\theta_{HRDPS}$ , was then reconstructed from the interpolated HRDPS wind components,  $u_{HRDPS\_int}$  and  $v_{HRDPS\_int}$ . This direction was used to select the two sets of precomputed micro-scale wind components or the wind directions  $\varphi_1$  and  $\varphi_2$  that bounds  $\theta_{HRDPS}$  (i.e.,  $\varphi_1 < \theta_{HRDPS} < \varphi_2$ ). These selected microscale wind components including the local terrain effect were then linearly interpolated and recombined to obtain the downscaled wind direction  $\theta_{Down}$ . The transfer functions corresponding to the wind directions  $\varphi_1$  and  $\varphi_2$  were also linearly combined to obtain the final transfer function,  $f_{down}$ . It was finally applied to scale the modulus of the interpolated HRDPS wind speed and derive the final downscaled wind speed as in Barons et al. (2018):

$$U_{Down} = f_{down} \sqrt{u_{HRDPS\_int}^2 + v_{HRDPS\_int}^2} \quad (2)$$

Wind speeds were then adjusted to 10-m wind speeds using the Prandtl-von Kármán logarithmic wind profile and modified to include vegetation interactions using the vegetation cover of the triangle as defined in Sect 2.2.1. Fetch effects due to the presence of upstream vegetation are not taken into account when adjusting the wind speed.

Forthofer et al. (2014) and Wagenbrenner et al. (2016, 2019) have shown that the mass-conserving version of WindNinja has difficulties simulating lee-side recirculation where flow separation occurs. This difficulty is due to the absence of a momentum equation in the WindNinja flow simulation (Forthofer et al., 2014). As lee-side flow strongly influences snow accumulation (e.g. Gerber et al., 2018), an additional and optional step was added to the wind downscaling procedure described above. It consisted of a modification of the transfer functions  $f_{down}$  to reduce wind speed in leeward areas prone to flow separation. At each CHM time step, leeward areas were identified using the Winstral topographic parameter  $S_x$  (Winstral and Marks, 2002;

290 Winstral et al., 2017), computed at each triangle using the downscaled wind direction,  $\theta_{Down}$ . The  $S_x$  algorithm examines all triangles along a fixed search line emanating from the triangle of interest to determine which triangle has the greatest upward slope relative to the triangle of interest. Positive  $S_x$  values indicate sheltering features whereas negative  $S_x$  values indicate that the triangle of interest height is the highest cell along the search line and is topographically exposed. In this study, the  $S_x$  algorithm used a search distance of 300 m, as in Winstral et al. (2017). Triangles with  $S_x$  values larger than  $20^\circ$  were considered  
295 susceptible to flow separation in agreement with previous studies on the onset of flow separation in complex terrain (e.g., Wood, 1995). For these triangles, the transfer function,  $f_{down}$  was set to a value of 0.25 (Winstral et al., 2009). Note finally that a mass and momentum-conserving version of WindNinja is also available (Wagenbrenner et al., 2019). Wagenbrenner et al. (2019) have shown that momentum-conservation improved flow simulation at windward and leeward locations compared to the mass-conserving version but numerical instabilities made this version of the code unusable in the complex topography of  
300 the Canadian Rockies.

### 2.2.5 Model experiments

A set of CHM experiments were designed to assess the effect of the wind field downscaling, and the impact of process representation on snowpack simulations at snowdrift-permitting scales (Table 2). A reference CHM configuration including wind downscaling accounting for recirculation, and gravitational and blowing snow redistribution was first defined (*WndTr Av Rc*). A stepwise model falsification was then used, removing the following processes from the model: (i) recirculation  
305 effects in the wind downscaling procedure (*WndTr Av NoRc*), (ii) blowing snow redistribution with PBSM-3D (*NoWndTr Av*), (iii) gravitational snow redistribution with SnowSlide (*NoWndTr NoAv*), (iv) wind downscaling with WindNinja (*No Down*). Note that all the CHM experiments considered in this study account for the effects of terrain slope and aspect on incoming shortwave radiation. These simulations covered the period from 1<sup>st</sup> September 2017 to August 31<sup>st</sup> 2018 to fully capture snow  
310 accumulation and ablation in the region. For each experiment, CHM outputs were rasterized to a 50 m x 50 m raster for model evaluation. This rasterization was done via the GDAL rasterization capabilities (GDAL/OGR contributors, 2020). In short, this algorithm takes the triangle geometry in conjunction with an output raster (with given cell sizes and domain extent) and resolves which raster cells correspond to each triangle. On the case that two triangles share an output cell, an overwrite is used by the algorithm. The 50 m x 50 m area was selected as it corresponds to the minimal triangle area for high-resolution used in  
315 this study (Table 1).

## 2.3 Data and evaluation methods

### 2.3.1 Meteorological observations

Hourly meteorological data collected at CRHO stations were used to evaluate the precipitation and wind fields driving CHM (Table 3). These stations include those in Marmot Creek Research Basin (Fang et al., 2019) and Fortress Mountain Snow  
320 Laboratory (Harder et al., 2016) (Table 3 and Fig. 1); covering an elevation range from 1492 m to 2565 m. Table 3 also

provides the Topographic Position Index (TPI) at the position of the stations (Table 3) as this metric provides a quantification of each station's elevation relative to its surrounding. In this study, TPI was defined as in Winstral et al. (2017) and consists of the difference between each station's elevation on a 50-m raster minus the mean of all pixel elevations located within a 2-km radius from the station. Hourly meteorological data were obtained from quality-controlled 15-min observations using the same method as in Fang et al. (2019). In particular, solid precipitation data were corrected from wind-induced undercatch using the method proposed by Smith (2007). Simulated wind speeds were corrected to the sensor height of each station (including snow depth) using a standard log-law for the vertical profile of wind speed near the surface and an aerodynamic roughness of 1 mm typically found in snow-covered alpine terrain (e.g., Naaim Bouvet et al., 2010).

### 2.3.2 Airborne LiDAR snow depth data

Airborne laser scanning (ALS) surveys were performed over the Kananaskis region on 5 October 2017 (late summer scan) and on 27 April 2018 (winter scan) using a Riegl Q-780 infrared (1024 micron) laser scanner with a dedicated Applanix POS AV Global Navigation Satellite System (GNSS) inertial measurement unit (IMU). The Q-780 scanner was flown at heights of approximately 2500 m above the terrain that yielded swath widths of 2000 m to 3000 m. Post-processing of the ALS survey flight trajectory yielded vertical and horizontal positional uncertainties of  $\pm 15$  cm ( $1\sigma$ ). Post-processed point clouds data were exported into LAS files, and LAStools (<https://rapidlasso.com/lastools/>) was used to generate 5 m resolution digital elevation models (DEMs). The summer and winter DEMs were co-registered to minimize slope and aspect-induced errors (Nuth and Kääb, 2011). Additional details about the processing workflow over snow-covered terrain can be found in Pelto et al. (2019). To estimate uncertainties on the snow depth retrieval, snow-free areas that included peaks and road surfaces were identified in a 3-m satellite imagery (Planet Scope) for 27 April 2018. Analysis of elevation change over these snow-free surfaces (34 comparison points across all elevation) indicated an average (median) elevation change of -4.1 cm (0.5 cm) and a standard deviation of 19.8 cm. The median absolute deviation reached 8.0 cm. The DEM of snow depth was masked to only include non-glacierized terrain (Fig. 1b) and to exclude any areas of elevation change that was less than 0 m and greater than 20 m; elevation change beyond these values are considered outliers (Grünewald et al., 2014) and can arise from steep terrain that was effectively in the shadow of the laser scanner. For model evaluation, the 5-m snow depth map was then resampled over the same 50-m raster as the CHM output, taking for each cell of the 50-m raster the average of all non-masked cells in the 5-m snow depth map. Cells of the 50-m raster that contained more than 75 % of masked cells in the 5-m snow depth map were masked out. In addition, grid points covered by glaciers identified in the Randolph Glacier Inventory (Pfeffer et al., 2014) were removed from the analysis since elevation change over these surfaces is also influenced by ice dynamics (Pelto et al., 2019). Finally, forested pixels identified using the global database of Hansen et al. (2013) at 30-m grid spacing were masked out as well since this study focuses on snow redistribution processes in open terrain.

The distributions of simulated and observed snow depths were compared for different 200-m elevation bands for three sub-areas of the Kananaskis domain (Fig. 1b): (i) Kananaskis North; (ii) Kananaskis South and; (iii) Haig. These three sub-areas were characterized by different mean (standard deviation) observed snow depths: 0.90 m (0.82 m) for Kananaskis North, 1.32

m (1.03 m) for Kananaskis South and 2.00 m (1.33 m) for Haig. For each elevation band, the Root Mean Squared Error (RMSE) and the Wasserstein distance of order 1,  $W_1$ , (Rüschendorf, 1985) were used to quantify the agreement between the simulated and the observed distributions.  $W_1$  is defined as:

$$W_1(s, o) = \int_{-\infty}^{+\infty} |S(s) - O(o)|$$

where  $s$  and  $o$  are the simulated and observed snow depth distributions and  $S$  and  $O$  the corresponding cumulative distribution functions.  $W_1$  has the same unit as the variable considered (here m for snow depth) and a perfect match between the distribution lead to  $W_1 = 0$ . For each sub-area, simulated and observed snow depth distributions were also compared as a function of slope orientation in the upper slopes using bias and  $W_1$  to provide a specific assessment of model performances in regions particularly exposed to wind-induced snow-transport. Upper slopes in the 50-m raster were identified using the TPI as defined above. Regions with TPI greater than 150 m were classified as upper slopes.

### 2.3.3 Sentinel-2 snow cover maps.

Wayand et al. (2018) suggested that snow persistence indices from Sentinel-2 images present a strong potential for the evaluation of distributed snow models in mountainous area. Hence, maps of the snow-covered area from the Copernicus Sentinel-2 satellite mission (Drusch et al., 2012) at 20-m resolution and at 5-day revisit time were considered as complementary data to evaluate CHM simulations. Sentinel-2 images from 1<sup>st</sup> September 2017 to 31<sup>st</sup> August 2018 were processed using the snow retrieval algorithm that is currently used to produce the Theia snow collection (Gascoïn et al., 2019). First, orthorectified top-of-atmosphere (level 1C) products were processed to bottom-of-atmosphere reflectances (level 2A) using the MAJA software version 3.1 (Hagolle et al., 2017). MAJA output cloud mask and flat-surface reflectances were used as input to the LIS software version 1.5. The LIS algorithm is based on the Normalized Difference Snow Index (Dozier, 1989) and uses a digital elevation model to better constrain the snow detection (Gascoïn et al., 2019). Hansen et al. (2013) global forest product was used to mask out pixels with a tree cover density larger than 50% since the snow retrieval algorithm is not adapted to the detection of the snow cover in dense forest areas where the ground is obstructed by the canopy. To further avoid misclassifications due to forest obstruction or turbid water surfaces, the DEM was used to mask out pixels below 2000 m asl. The final snow product provided the following classification for each pixel: (i) no snow, (ii) snow, (iii) cloud, including cloud shadows and (iv) no data.

Sentinel-2 snow cover maps at 20-m resolution were resampled to the same 50-m raster as the CHM output using a median filter. Maps of observed snow persistence (SP) indices at 50-m resolution were then derived following Macander et al. (2015) and Wayand et al. (2018). SP represents for each pixel the ratio between the number of snow-covered days divided by the total number of clear-sky observations (snow or no-snow). SP was computed using images from 1<sup>st</sup> April 2018 to 31<sup>st</sup> August 2018 and SP ranges from 0 (always snow-free) to 1 (always snow-covered). Over the study period, the mean number of clear-sky observations per pixel reached 18.6 days. The same calculation was carried out with CHM outputs to derive maps of simulated snow persistence indices. The same dates as the Sentinel-2 maps were used and for each date, the Sentinel-2 cloud and no-data

masks were applied to make sure that the same pixels and dates were considered when computing observed and simulated SP indices. A grid cell was considered snow-covered if the snow thickness exceeded 5 cm (Gascoin et al., 2019). The agreement between the simulated and the observed SP distributions was quantified as a function of elevation and slope orientation in the upper slopes for the three same sub-regions considered for snow depth (i.e., Kananaskis North, Kananaskis South, and Haig).  
390 Grid cells that were not covered by forest in the observations and in the simulations were considered for the analysis.

### 3. Results

The evaluation of the different wind downscaling methods is described in Sect. 3.1. The quality of the snowpack simulations is then assessed in Sect. 3.2 using airborne LiDAR snow depth data and snow persistence indexes. A special emphasis is placed on the ability of the model to capture the elevation-snow depth relation as well as snow redistribution around wind-exposed  
395 ridges.

#### 3.1 Wind field downscaling

Figure 3 compares the near-surface wind field obtained from a simple bilinear interpolation of the HRDPS wind field (Fig. 3a) with the downscaled wind field obtained with (Fig. 3c) and without (Fig. 3b) the wind speed reduction in leeward areas. HRDPS provided a smooth wind field with relatively higher wind speeds in the northwestern part of the region characterized  
400 by high relief (Fig 3a) compared to the rest of the area. HRDPS did not reflect the local terrain information due to a horizontal resolution of 2.5 km. Combining the HRDPS wind field with precomputed microscale WindNinja simulations strongly altered the near-surface wind field (Fig. 3b). The downscaled field contained the general pattern from the HRDPS modulated by the local-scale terrain information added by WindNinja and reproduced some typical features of atmospheric flow in complex terrain (e.g., Raderschall et al., 2008). In particular, the topography surrounding the main valleys channeled the downscaled  
405 atmospheric flow, as illustrated by downscaled wind directions aligned parallel to the main valley axes. The presence of ridge crests generated cross-ridge downscaled flow and associated crest wind speed-up. Downscaled wind speeds were the same on the windward and leeward sides of crests, however, as expected with the mass-conserving version of Wind Ninja (Wagenbrenner et al., 2016; 2019). For this reason, an additional downscaling step using the Winstral parameter to reduce the wind speed in leeward areas was considered as described in Sect. 2.2.4 (Fig. 3c). Blue arrows on Fig. 3c correspond to leeward  
410 areas sheltered from the atmospheric flow and characterized by low downscaled wind speed. This additional downscaling step did not modify the wind direction in these areas.

Figure 4 gives the error metrics for the wind speed (Bias and RMSE) between the CHM simulations and observations at eight automatic weather stations. The HRDPS without downscaling overestimated wind speed (positive bias) at all stations, except the CNT station. This station is located on an exposed crest and presents the largest TPI value among the stations used for  
415 model evaluation (Table 3). Downscaling wind to the CHM mesh using WindNinja microscale winds (experiment HRDPS+WN) improved the error metrics (decrease in bias in absolute value and decrease in RMSE) at four of the stations

(BRP, HMW, FSR and CNT). In particular, the wind downscaling reduced the negative bias found in the HRDPS for the wind-exposed CNT station, presumably because the downscaling captures ridge crest speed-up of wind velocity. Decreased model performances were found at four neighbouring stations located around the Fortress Mountain Snow Laboratory, however  
420 (CRG, FRG, FRS and FLG; Fig 3a). At these stations located along local ridges, the wind downscaling, accounting for crest speed-up, increased the wind speed and led to a larger positive bias than the default HRDPS (Fig. 3b). Accounting for the formation of zones of low wind speed in leeward areas in the downscaling method (experiment HRDPS+WN+Rc) was neutral at two stations located at low elevation (BRP and HMW) and improved results at all remaining stations, except at CNT. Indeed, a strong degradation of model performance was found at this station since it is placed on a sheltered triangle next to the crest  
425 on the CHM mesh, leading to an unrealistic reduction of downscaled wind speed.

The wind downscaling method also modified the general wind direction (Figs. 3 and 5). Prevailing winds during the study originated from the South (S;  $180^\circ$ ) - South West (SW;  $225^\circ$ ) at most of the stations whereas the HRDPS without downscaling provided wind mainly from the SW - West (W;  $270^\circ$ ). Improvements in wind direction when combining HRDPS and WindNinja were found for about half of the meteorological stations. The large error at the CRG station illustrated that none of  
430 the wind simulation considered in this study captured the complex features of the atmospheric flow around the Fortress Mountain Snow Laboratory (Fig 3a).

## 3.2 Snowpack simulations

### 3.2.1 Observed and simulated snow distributions

To assess the ability of CHM to simulate small-scale features of snow accumulation and transport in alpine terrain, ALS-  
435 derived snow depths were compared with simulated snow depths for different CHM experiments for a sub-region of approximately  $77 \text{ km}^2$  (Fig. 6). Observed snow depth was characterized by strong spatial variability (Figure 6a). Shallow snow cover (generally less than 1 m) was found in the upper south- to northeast-facing slopes that were primary exposed to wind (Fig. 5). Snow accumulated on the leeward side of these slopes (purple contours on Fig. 6a). Thick snow cover ( $> 4 \text{ m}$ ) existed at the bottom of steep slopes and in large concave cirques corresponding to avalanche deposition areas (red contours  
440 on Fig. 6a). The CHM simulation without lateral redistribution of snow (blowing snow and avalanching), *NoWndTr NoAv<sub>2</sub>* did not capture these features (Fig 6d). CHM without blowing snow and avalanche routines simulated a homogenous snow cover with reduced snow accumulation for some of the crest regions that are exposed to wind and prone to large surface snow sublimation. A better visual agreement with observations was found when accounting for gravitational snow redistribution in CHM (Fig. 6c). In this configuration, CHM partially reproduced reduced snow accumulation on steep slopes and avalanche  
445 deposits were simulated at the bottom of these slopes (red contour on Fig. 6c). However, the model mostly underestimated the snow depth in these deposits compared to the observations (red contours on Fig. 6a) and did not capture the snow depth distribution in the upper slopes (purple regions on Fig. 6c). The reference CHM with lateral redistribution of snow and wind speed reduction in leeward slopes, *WndTr Av Rc*, brought large improvements (Fig. 6b). Accounting for blowing snow

redistribution reduced snow accumulation on windward slopes and locally increased snow deposition in the upper parts of  
450 leeward slopes (purple contours on Fig. 6b). It also led to a large increase in snow accumulation in avalanche deposition areas  
(red contours on Fig. 6b) that better corresponded with observed features of snow accumulation (Fig. 6a). However, *WndTr  
Av Rc* presented an overestimation of snow depth in some of the large valleys of the region (blue contours on Fig. 6) where  
avalanche deposition seemed to be overestimated.

### 3.2.2 Elevation-dependency of snow depth

455 The agreement between observed and simulated snow depth distributions was examined as a function of elevation for three  
sub-regions (see Fig. 1) of the Kananaskis domain: Kananaskis North, Kananaskis South and Haig (Fig. 7 and 8). For each  
sub-region, the median of observed snow depth increased with elevation up to 2400 m followed by a decrease at the highest  
elevations (Fig. 7), a relationship reported elsewhere (Grünewald et al., 2014; Kirchner et al., 2014). The same trend was found  
460 for the other percentiles shown on the whisker plots of the observed distributions of snow depth (Fig. 7). All CHM simulations  
overestimated the snow depth below 2100 m for each sub-region, partly explained by the tendency of HRDPS to overestimate  
precipitation at valley stations (see stations HMW and UPC on Fig. S1 in the supplementary material). The CHM simulation  
without lateral redistribution of snow (*NoWndTr NoAv*) did not capture the observed spatial variability within each elevation  
band (Fig. 7). Instead, simulated average snow depth increased with elevation and diverged with observed decreased snow  
465 depth recorded with the ALS survey. Therefore, the experiment *NoWndTr NoAv* presented an increase of the Wasserstein  
distance and RMSE with elevation (Fig. 8) associated with a continuous decrease in model performance with increasing  
elevation. Accounting for gravitational redistribution in CHM (experiment *NoWndTr Av*; orange boxes in Fig. 7) increased the  
spatial variability within each elevation band and reduced snow accumulation above 2400 m, especially for the Haig sub-  
region (Fig. 7c) characterized by steep slopes prone to avalanching (Fig. 1b). The experiment *NoWndTr Av* led to improved  
Wasserstein distance at all elevation for each sub-region compared to the experiment *NoWndTr NoAv* (Fig. 8). Snow depth  
470 above 2300 m for all sub-regions was still overestimated, however (Fig. 7). The increase in RSME below 2400 m (Fig. 8)  
suggested that experiment *NoWndTr Av* did not capture the location of avalanche deposits well.

Including blowing snow redistribution strongly affected model results. As expected, it increased the spatial variability of  
simulated snow depth within each elevation band compared to experiments *NoWndTr NoAv* and *NoWndTr Av* (Fig. 7). When  
the wind speed reduction in leeward areas was not simulated (experiment *WndTr Av NoRc*), CHM underestimated the median  
475 snow depth (as well as the 1<sup>st</sup> and 3<sup>rd</sup> quartile) above 2500 m compared to observations. This underestimation increased with  
elevation and was largest for the elevation band 2900-3100 m. Including the recirculation effect when simulating blowing  
snow (experiment *WndTr Av Rc*) strongly improved the ability of the model to capture the distribution of snow depth at high-  
elevation (above 2700 m for Kananaskis North, Fig. 8a; above 2500 m for Kananaskis South, Fig. 8b and above 2100 m for  
Haig, Fig. 8c). Overall, the experiment *WndTr Av Rc* captured the observed shape of the elevation-snow depth relation for  
480 each sub-region (Fig. 7). Below 2300 m, experiments *WndTr Av NoRc* and *WndTr Av Rc* overestimated the value of the 95<sup>th</sup>  
percentile of the snow depth distribution compared to observations (Fig. 7). These two configurations of CHM also led to a

larger Wasserstein distance (between 1900 m and 2100 m) and larger RMSE (below 2500 m) compared to experiments *NoWindTr NoAv* and *NoWindTr Av*. These results are consistent with the overestimation of gravitational snow redistribution to lower elevation and the erroneous location of avalanche deposits observed on Fig. 6b.

### 485 3.2.3 Snow distribution around ridges

The observed and simulated snow depth distributions were compared for the upper slopes of the domain (defined in Sect. 2.3.2), particularly exposed to wind-induced snow transport (Fig. 9). The CHM simulation without lateral redistribution of snow, *NoWindTr NoAv*, presented a systematic overestimation of snow depth for all slope orientations (Fig. 9, Top) and yielded the worst Wasserstein distance metric among all simulations (Fig. 9, Bottom). Including gravitational redistribution reduced the positive bias and the Wasserstein distance. This reduction was not found for some slope orientations, however (W, SW and S orientations for Kananaskis North, Fig. 9a, and SW and S orientations for Kananaskis South, Fig 9b). The moderate values of the slope angle generally found for these orientations were not sufficient to trigger gravitational snow redistribution in SnowSlide. For example, the percentage of slope values larger than  $40^\circ$  is only 9% for the SW and S orientations for Kananaskis North, compared to 43% and 63% for the N and NE orientations for the same region, respectively. Accounting for blowing snow redistribution without wind speed reduction in leeward areas generated a systematic underestimation of snow depth for all slope orientations and sub-regions (Fig. 9, Top). This negative bias in snow depth indicates that snow erosion on the windward slopes (S to NW orientations) was overestimated for experiment *WindTr Av NoRc*. Thinner-than-observed snow depth on the upper part of the leeward slopes (N to SE orientations on Fig. 9, Top) suggests that the wind-blown snow eroded in excess from the windward slopes was transported by PBSM-3D to the lower part of the leeward slopes due to the absence of wind recirculation in the driving wind field used by experiment *WindTr Av NoRc* (Fig. 3b). A similar underestimation of snow depth on the windward slopes exists for experiment *WindTr Av Rc*. Due to the activation of the wind speed reduction in leeward areas, however, this experiment simulated snow deposition in the upper part of these areas. The experiment *WindTr Av NoRc* led to an overestimation of snow depth on the leeward slopes for Kananaskis North and South (N to SE orientations, Fig. 9a b) and nearly unbiased estimation of snow depth for Haig (NE to SE orientations, Fig. 9c). Overall, experiment *WindTr Av Rc* provided the best performances in term of Wasserstein distance for the windward slopes of all sub-regions (Fig 9. Bottom) despite the negative bias in snow depth for these areas. Performances were more mixed for leeward slopes: Haig showed an improvement compared experiment *NoWindTr Av* (Fig. 9f) whereas worst performances were obtained for Kananaskis North (Fig. 9d).

### 3.2.4 Snow Persistence

510 Figure 10 shows the maps of observed snow persistence indexes as well as the indexes derived from two CHM simulations. Observed SP (Fig. 10a) presented similar patterns compared to the observed distribution of snow depth in late April (Fig 6a), showing that snow persistence patterns are primarily controlled by the patterns of peak snow accumulation (Wayand et al., 2018). Avalanche deposits identified on Fig. 6a corresponded to maximal SP values whereas low SP values were found near



ridges lines, exposed to wind. Overall, the Pearson correlation coefficient between observed snow depth and SP reached 0.69 (p <0.001), 0.68 (p<0.001) and 0.75 (p<0.001) for Kananaskis North, Kananaskis South and Haig, respectively. Without accounting for lateral snow redistribution (experiment *NoWndTr NoAv*), CHM-simulation derived SP values were dependent upon the elevation and slope orientation (Fig. 10c), primarily due to the impact of solar radiation on simulated snow ablation. Without lateral snow redistribution, snow accumulation was spatially uniform (Fig. 6d and 7). Lower values of simulation derived SP were found in the lower south-facing slopes whereas steep slopes on northern faces had SP values close to 1.0. The simulation derived SP was strongly modified with experiment *WndTr Av Rc* (Fig. 10b), similarly to the effect found for snow depth near peak snow accumulation (Fig. 6b). In this experiment, windward slopes systematically presented low SP values and maximal SP values close to 1.0 were found at the bottom of slopes due to gravitational redistribution of snow that prevented from snow persistence on steep slopes.

Figure 11 shows how accurately the different CHM experiments were able to reproduce the observed SP distributions as a function of elevation. The simulation derived and observed SP distributions are shown on Fig. S2. Model performances for snow persistence were generally in agreement with those for snow depth presented at Fig. 8. Experiments without blowing snow redistribution (*NoWndTr NoAv* and *NoWndTr Av*) overestimated snow persistence at all elevations with a positive bias increasing with elevation for experiment *NoWndTr NoAv*. Including blowing snow redistribution in experiments *WndTr Av NoRc* and *WndTr Av Rc* significantly decreased snow persistence, mainly above 2300 m. The absence of wind speed reduction in leeward areas (experiment *WndTr Av NoRc*) led to negative bias of snow persistence above 2700 m and a decrease in model performances compared to experiment *WndTr Av Rc* that includes recirculation effects. Below 2500 m, experiments *WndTr Av NoRc* provided the best performances in terms of bias and Wasserstein distance. Consistent results compared to snow depth were also obtained when considering how observed and simulated SP distributions vary with slope orientation in upper slopes (Fig. 12). For example, the tendency of experiment *WndTr Av Rc* to overestimate snow accumulation on the leeward slopes of Kananaskis North led to a clear overestimation of snow persistence on these slopes (Fig. 12a) and a degradation of model performance compared to a simulation without blowing snow redistribution (Fig. 12d).

## 4. Discussions

### 4.1 Modelling of mountain snowpack

This study presents a new high-resolution modelling strategy for mountain snowpack combining atmospheric forcing from a NWP system at convection-permitting scale with the multi-scale, snowdrift-permitting model CHM. Several CHM configurations were tested to highlight how missing physical processes influenced the performances of snowpack simulations at snowdrift-permitting scales (50 m in this study). Lateral snow redistribution (blowing snow and avalanching) were required to capture natural variations in snow depth and its persistence, a finding that accords with Winstral et al. (2013) and Hanzer et al. (2016). These results differed from Revuelto et al. (2018) who showed that a distributed snowpack scheme without lateral snow redistribution can provide accurate estimation of snow cover variability. This discrepancy may arise from (i) the

550 resolution of 250 m used in Revuelto et al. (2018) for which lateral redistribution processes are partially sub-grid and (ii) the absence of ALS data and high-resolution satellite images to evaluate their snowpack simulations. Accounting for gravitational redistribution reduced snow accumulation and persistence in steep slopes in agreement with the findings of Bernhardt and Schulz (2010). This was not sufficient and snow depth and persistence were still overestimated for the upper slopes exposed to wind. The CHM simulation (*WndTr Av Rc*) that included blowing snow redistribution and avalanching was required to capture the decrease in snow depth at high-elevation (above 2500 m); it also improved the elevation-snow depth relationship for all sub-domains of the Kananaskis domain. Similar elevation-snow depth relationships presenting a snow depth maximum below the highest elevations have also been reported for other mountainous regions (Grunewald et al., 2014; Kirchner et al., 2014). Our results suggest that accounting for blowing snow redistribution and avalanching in distributed snowpack simulations is crucial to accurately simulating the elevation-snow depth relationships in high mountain terrain.

555 Results of blowing snow redistribution simulations in CHM were sensitive to the quality of the driving wind field, in particular the impact of recirculation areas, at the mountain range scale ( $> 100 \text{ km}^2$ ). This observation builds on the similar findings of Mott and Lehning (2010) and Musselman et al. (2015) based on ridge-scale simulations of snow depth. High-resolution wind fields obtained using the mass-conserving version of the diagnostic wind model WindNinja (Forthofer et al., 2014) presented some features of atmospheric flow in alpine terrain (e.g. valley channeling, crest speed-up) but they did not capture the formation of recirculation areas on leeward slopes. This lack of recirculation led to lower-than-observed snow deposition and persistence on leeward slopes. These results highlight the limitations of mass-conserving diagnostic wind models for blowing snow modelling in alpine terrain. Combining high-resolution wind fields from WindNinja with a terrain-based parameter (Winstral and Marks, 2002) allowed identifying potential areas of flow separation on leeward slopes and improved simulations of the elevation-snow depth relationship and of the snow distribution and persistence around ridges. This simulation was still impacted by an overestimation of snow erosion on windward slopes and subsequent deposition on leeward slopes, likely arising from uncertainties associated with the wind downscaling method and limitations in CHM parameterizations discussed in Sect. 4.3 and 4.4.

#### 4.2 Importance of high-resolution distributed evaluation data

570 The evaluation of the wind downscaling methods versus point measurements did not show systematic improvements compared to the original HRDPS wind field, consistent with studies of high-resolution wind modelling in complex terrain (e.g., Horvath et al., 2012; Vionnet et al., 2015). Model results in Sect. 3.1 highlight the challenge of evaluating wind simulations at locations near peaks or ridges due to approximation in the location of the stations as previously mentioned in Fiddes and Gruber (2014) and Winstral et al. (2017). On the other hand, differences between the wind downscaling methods were clearly identified and quantified when evaluating the snow simulations using distributed data. ALS snow depth and snow persistence indexes derived from Sentinel-2 allowed for targeted model evaluation in area of interest such as the upper slopes exposed to wind-induced snow transport. These results confirm the large potential of ALS snow depth data for detailed model evaluation (e.g., Hanzer et al., 2016; Hedrick et al., 2018). In addition, they show that snow persistence indexes derived from freely available Sentinel-

2 images (Wayand et al., 2018) can generally support similar conclusions than those derived from ALS snow depth. This  
580 highlights that these indexes can be used to evaluate large-scale snowpack simulations at snowpack-permitting scales in regions  
that are not covered by LiDAR. As illustrated by Wayand et al. (2018), the snow persistence index is influenced by variability  
in both snow accumulation and ablation, so that this index can only be used to evaluate snow redistribution models if variable  
insolation effects are also simulated. This is the case in the simulations presented in this paper (Sect 2.2.5).

Two types of metrics were used when using ALS snow depth data for model evaluation: RMSE and Wasserstein distance.  
585 RMSE corresponds to a traditional “point-to-point” verification metric. Such metric may favor homogenous snow cover  
simulations. Indeed, a snow cover simulation including avalanching may present a degree of realism but errors in the exact  
location of the avalanche deposits may increase RMSE compared to a simulation without avalanching due to the double-  
penalty problem (e.g., Nurmi, 2003). This issue is often encountered when evaluating the ability of high-resolution atmospheric  
model to simulate localized events such as convective precipitation (e.g., Clark et al., 2016). The Wasserstein distance  
590 (Rüschendorf, 1985) was used in this study as a complementary metric to evaluate the agreement between observed and  
simulated distributions for specific areas (elevation bands or specific slope orientations). This metric may lead to a perfect  
match even if the observations and the simulations are not co-located, however. This highlights the need to consider several  
verification metrics with identified strengths and limitations. In the future, more advanced verifications methods such as the  
neighborhood methods developed in the atmospheric community (Ebert et al., 2013) could be considered.

#### 595 **4.3 Uncertainties in the atmospheric driving data**

This study used a wind downscaling method inspired by Barcons et al. (2018) and developed for large areas. Part of the  
uncertainty associated with this method comes from the value of the radius of influence used to compute the transfer functions  
(Sect. 2.2.4). A value of 1 km was selected for this study, similar to Barcons et al. (2018) as the resolutions of the mesoscale  
atmospheric models were similar between the two studies (2.5 km in this study and 3 km in Barcons et al., 2018). Further work  
600 is required to adapt this value to the resolution of the mesoscale atmospheric models and to the terrain complexity. Sensitivity  
tests revealed that the wind field in the upper slopes strongly depend on the value of the radius of influence with a potential  
large impact on simulated snow redistribution. The accuracy of the wind downscaling was also influenced by the quality of  
the diagnostic wind model used to generate microscale wind fields. In particular, the mass-conserving version of WindNinja  
used in this study failed to simulate the formation of recirculation areas on leeward slopes that are one of the main features of  
605 atmospheric flow in alpine terrain (Raderschall et al., 2008; Gerber et al., 2017). The practical method relying on the Winstral  
parameter (Winstral and Marks, 2002) proposed to overcome this limitation is affected by strong assumptions on the value of  
the critical angle for flow separation (Wood, 1995). Gerber et al. (2017) showed that atmospheric stability affects the value of  
this angle and the development of leeside recirculation. A constant value of 0.25 is used for the transfer function in recirculation  
zones. This value falls within the range of values reported on Fig. 10 of Menke et al. (2019) for the ratio,  $R$ , between the  
610 maximum wind speed in recirculation flow and the inflow wind speed at the crest. Menke et al. (2019) found that  $R$  tends to  
decrease with increasing stability in a stable atmosphere and it presents values lower than 0.3 for inflow wind speed greater

than  $12 \text{ m s}^{-1}$ . This suggests that a dynamic value based on atmospheric stability could be used for the transfer function in recirculation zones. In addition, the wind direction is not modified in these areas, contrary to simulations resulting from CFD models or atmospheric models in LES mode (Gauer, 1998; Mott and Lehning, 2010; Vionnet et al., 2017). Improvements in  
615 the wind downscaling could be achieved using such models to generate the library of wind fields, as proposed by Barcons et al. (2018). Different conditions of atmospheric stability could also be considered (e.g., Gerber et al., 2017) as well as different input wind speeds that affect significant flow features such as flow separation. Final selection of the wind downscaling strategy will ultimately be a trade-off between model complexity, accuracy and computational costs and will vary as a function of model applications.

620 All the atmospheric driving data for CHM were obtained from the HRDPS, the Canadian NWP system using GEM at 2.5 km (Milbrandt et al., 2016). It consisted of successive short-range forecasts combined to generate a continuous atmospheric forcing. Such approach has been used previously to generate atmospheric forcing for snowpack models in mountainous terrain (Horton and Jamieson, 2016; Quéno et al., 2016; Vionnet et al., 2016; Luijting et al., 2018). Error in the snowpack variables can grow with time due to errors in the successive forecasts, especially those due to precipitation biases (e.g., Vionnet et al.,  
625 2019). Errors in the longwave and shortwave radiative input can also significantly affect snowpack simulations (Lapo et al., 2015; Quéno et al., 2020). The downscaling techniques used to adapt the HRDPS forcing to the CHM mesh likewise contribute to the uncertainty in the quality of the meteorological input. Monthly fixed altitudinal gradients were used to adjust the near-surface temperature and humidity forcing; this method might be further improved using upper-air HRDPS temperatures and humidity fields (e.g., Jarosch et al., 2010; Fiddes et al., 2014). Contributions from the surrounding topography to longwave  
630 irradiance were also neglected, despite its impact on the snowpack energy balance on inclined slopes (Pluss and Ohmura, 1997). Ensemble simulations based on ensemble meteorological forcing (e.g., Vernay et al., 2015) and ensemble downscaling methods (Marsh et al., 2020a) could be used to investigate the impact of these sources of uncertainties.

#### 4.4 Limitations in the physical parameterizations in CHM

The model evaluation for the upper slopes exposed to wind showed that CHM simulations including blowing snow tend to  
635 overestimate snow-redistribution across slopes subject to wind erosion and deposition. These results were obtained for a CHM mesh with a typical area of  $50 \text{ m} \times 50 \text{ m}$  near the crest lines. Mott and Lehning (2010) found a similar overestimation of snow-redistribution in simulations of the snow cover evolution for a crest of the Swiss Alps using the Alpine 3D model (Lehning et al., 2008) running at 50-m grid spacing. They showed that increasing the model resolution finer than 10 m increased snow accumulation on windward side due a more accurate representation of small-scale terrain features trapping snow on the  
640 windward side. These results suggest that the absence of any subgrid topography effects on snow transport in CHM can partially explain the overestimation of snow redistribution from windward slopes to leeward slopes and subsequent avalanching. In addition, CHM uses the formulation for the threshold friction velocity for snow transport of Li and Pomeroy (1997) that only depends on snow presence and air temperature. Though based on a large multi-year observational dataset, such parameterization is empirical and does not also account for the effect of snow fragmentation during blowing snow events

645 (Comola et al., 2017) which may lead to an underestimation of the threshold friction velocity and an overestimation of blowing  
snow occurrence in alpine terrain (Vionnet et al., 2013). CHM may benefit from the inclusion of a more physically based snow  
transport routine in the future. Finally, CHM uses a thickness of 5-m for the suspension layer (Marsh et al., 2020a). This is  
sufficient to capture most of the mass transported in alpine terrain over slopes exposed to wind with limited fetches (Pomeroy  
et al. 1993; Naaim Bouvet et al, 2010) but it cannot simulate the formation of snow plumes at crest lines. Mass loss due to the  
650 advection of blown snow particles to atmospheric layers and subsequent sublimation are likely underestimated by CHM. Such  
a limitation is also found for more advanced blowing snow schemes (see for example Fig. 6 of Groot Zwaaftink et al., 2011  
and Fig. 8.6 of Vionnet, 2012).

Gravitational snow redistribution is simulated in CHM with the SnowSlide scheme (Bernard and Schulz, 2010). Model results  
showed that CHM can reproduce the formation of snow accumulations due to avalanching that visibly correspond with the  
655 observations. However, the increase in RMSE for snow depth at low elevation for all simulations including avalanching  
suggests that CHM does not effectively capture the true location of these deposits. SnowSlide relies on a maximum holding  
capacity of snow that only depends on the slope angle and does not consider the small-scale terrain roughness, limiting the  
ability of the scheme to reproduce snow accumulation for steep faces (Sommer et al., 2015). In addition, the exact location of  
avalanche deposits is influenced by avalanche dynamics (Pudasaini and Hutter, 2007) which are not reproduced in SnowSlide.  
660 CHM also does not represent snowfall enhancement due to interactions between the flow field and the local cloud formation  
as well as the preferential deposition of snowfall resulting from pure particle flow interaction (Lehning et al., 2008; Vionnet  
et al., 2017; Mott et al., 2018). Gerber et al. (2019) suggested that, when combined, these two effects can increase snow  
accumulation on the leeward side of mountain ridges by 26-28%. In the current version of CHM, wind-induced snow transport  
is the only process responsible for additional snow deposition on leeward slopes. The parameterization of Dadic et al. (2010)  
665 could be tested in CHM but would require an estimation of the vertical wind speed that could be provided by WindNinja. A  
study is in progress in the Canadian Rockies to better assess the impact of terrain–flow–precipitation interactions on snow  
accumulation in the region. Finally, uncertainties associated with the Snobal snowpack scheme were not quantified in this  
study. In particular, errors in simulated snow density can affect the comparison between observed and simulated snow depth  
(Raleigh and Small, 2017; Lv and Pomeroy, 2020), despite the use of an improved snow density algorithm for Snobal (Hedrick  
670 et al., 2018). Inaccurate estimations of the ground heat flux may also affect the simulation of the snow cover duration (Slater  
et al., 2017). Pritchard et al. (2020) showed how multi-physics ensemble snow modelling can be applied to assess uncertainties  
on distributed snowpack simulations and a similar framework could be applied to CHM, including uncertainties in PBSM-3D  
and SnowSlide.

## 5. Conclusions

675 This study presents a new multi-scale modeling strategy of mountain snowpack over large regions. It combines (i) atmospheric  
forcing from the Canadian GEM NWP system at a convective-permitting scale (Milbrandt et al., 2016), (ii) a meteorological

downscaling module including a wind downscaling strategy relying on the diagnostic wind model WindNinja (Forthofer et al., 2014) and (iii) the multi-scale snowdrift-permitting model CHM (Marsh et al., 2020a, b). This system was used to simulate the snowpack evolution for an entire snow season over a domain of 958 km<sup>2</sup> in the Kananaskis Valley of the Canadian Rockies.

680 Wind simulations were evaluated using data from automatic stations in the domain. The distributed evaluation data for the snowpack simulations consisted of maps of snow depth derived from airborne LiDAR and snow persistence indexes derived from optical satellite imagery. Several configurations of CHM were tested to assess the effect of the wind field downscaling, and the impact of process representation on snowpack simulations at snowdrift-permitting scales.

The main conclusions of this study are that:

- 685 • Pre-computed wind fields at 50-m grid spacing with the WindNinja model can be combined efficiently with output of the Canadian NWP system at 2.5 km grid spacing to produce hourly driving wind fields including small-scale topographic features. The mass conserving version of WindNinja used in this study cannot reproduce leeside flow recirculation, however. The Winstral terrain parameter,  $S_x$ , provides a solution to identify potential recirculation areas and adjust accordingly the wind field downscaled with WindNinja.
- 690 • Snowpack simulation without lateral snow redistribution (blowing snow and gravitational snow redistribution) cannot capture the spatial variability of snow cover in alpine terrain and overestimates snow depth and snow cover duration at high elevations. Including gravitational redistribution improved model results and reduced snow depth at high elevations. Snow depth and snow cover duration was still overestimated around ridge lines exposed to winds.
- 695 • Snowpack simulation including blowing snow and gravitational snow redistribution provided the best estimates of the shape of the elevation-snow depth relation across the Kananaskis region and reproduced the decrease in mean snow depth found at high elevation. These results were obtained for a CHM experiment driven by a wind field including the wind speed reduction in leeward areas. Removing these zones led to a systematic underestimation of snow depth around ridges, partially due to an underestimation of snow deposition on leeward slopes. These results highlight that wind fields without lee-side slowdown are not sufficient to simulate snow redistribution in mountainous terrain.
- 700 • Snowpack simulations including blowing snow and gravitational snow redistribution overestimated snow redistribution from windward to leeward slopes and subsequent avalanching. This is potentially due to the absence of subgrid topographic effects in the driving wind field and in the snow transport equations in CHM.
- 705 • High-resolution snow persistence indexes derived from Sentinel-2 presents a strong potential for the detailed evaluation of distributed snowpack models, in particular in regions where Airborne LiDAR snow depth data are not available. These indices can be used for model evaluation targeting specific areas (e.g. ridges lines exposed to intense wind-induced snow redistribution, avalanche deposition areas).

The results of this study demonstrate that CHM at snowdrift-permitting scale constitutes a promising tool for large-scale modelling of mountain snowpack. Future work will combine (i) improvements in the physical parameterizations in CHM and

710 in the driving wind fields, (ii) large scale simulations across the Western Canadian Cordillera, and (iii) improvements of CHM simulations with assimilation of high-resolution observations such as ALS snow depth or Sentinel-2 snow cover.

### **Code availability**

715 The open-source CHM model code (Marsh et al., 2020b) is available at <https://github.com/Chrismarsh/CHM>. The *mesher* algorithm (Marsh et al., 2018) is available at <https://github.com/Chrismarsh/mesher>. The high-resolution wind library has been generated using the WindNinja diagnostic wind model (Forthofer et al., 2014; <https://weather.firelab.org/windninja/>) and the Windmapper tool (<https://github.com/Chrismarsh/Windmapper>). The Sentinel-2 snow cover maps were generated from level 1C images using the free software MAJA (<https://logiciels.cnes.fr/en/content/maja>) and the open source software LIS ([https://gitlab.orfeo-toolbox.org/remote\\_modules/let-it-snow/](https://gitlab.orfeo-toolbox.org/remote_modules/let-it-snow/)).

### **Data availability**

720 CRHO meteorological and snow observations are available through the web portal <http://giws.usask.ca/meta/>. HRDPS forecasts are distributed on the Canadian Surface Prediction Archive (CaSPAR; <https://caspar-data.ca/>). Sentinel-2 level 1C data were obtained from the Plateforme d'Exploitation des Produits Sentinel (<https://peps.cnes.fr>). Final snow cover maps over the Kananaskis Valley are available on Zenodo (Gascoin, 2020). The HRDPS forcing file and the ALS data used in this study are available on request to the authors.

### **725 Author contribution**

VV, CM, BM and JP designed the study and the modelling strategy. VV and CM developed the wind downscaling module in CHM. VV was responsible for the analysis of the results and the preparation of the manuscript. BM, JS, and KM processed and provided the Airborne-LiDAR snow depth data. SG processed and provided the Sentinel2 snow cover images. NW provided a pre- and post-processing toolkit for CHM. All authors contributed to the preparation of the manuscript.

### **730 Competing interest**

The authors declare that they have no conflict of interest.

### **Acknowledgements**

This study was supported by the Global Water Future programme funded by the Canada First Research Excellence Fund. Support from the Canadian Foundation for Innovation, Canada Research Chairs Program, NSERC and Tula Foundation is

735 gratefully acknowledged. Martyn Clark (USask) and Barbara Casati (ECCC) are thanked for their helpful scientific discussions. Special thanks to Logan Fang (USask) and Greg Galloway (USask) for providing quality-controlled snow and meteorological data. SG acknowledges the Centre National d'Etudes Spatiales (CNES) for granting him access to its high-performance computer. We thank Rebecca Mott and Tobias Sauter for their careful reading and useful comments, which improved the manuscript.

## 740 **References**

- Baba, M. W., Gascoin, S., and Hanich, L.: Assimilation of Sentinel-2 data into a snowpack model in the High Atlas of Morocco. *Remote Sensing*, 10, 1982, <https://doi.org/10.3390/rs10121982>, 2018
- Barcons, J., Avila, M., and Folch, A.: A wind field downscaling strategy based on domain segmentation and transfer functions. *Wind Energy*, 21, 409-425, <https://doi.org/10.1002/we.2169>, 2018
- 745 Bernhardt, M., and Schulz, K.: SnowSlide: A simple routine for calculating gravitational snow transport. *Geophys. Res. Lett.*, 37, <https://doi.org/10.1029/2010GL043086>, 2010
- Bernhardt, M., Liston, G. E., Strasser, U., Zängl, G., and Schulz, K.: High resolution modelling of snow transport in complex terrain using downscaled MM5 wind fields. *The Cryosphere*, 4, <https://doi.org/10.5194/tc-4-99-2010>, 2010
- Brauchli, T., Trujillo, E., Huwald, H., and Lehning, M.: Influence of slope-scale snowmelt on catchment response simulated with the Alpine3D model, *Water Resour. Res.*, 53, 10723-10739, <https://doi.org/10.1002/2017WR021278>, 2017
- 750 Clark, M. P., Hendrikx, J., Slater, A. G., Kavetski, D., Anderson, B., Cullen, N. J., Kerr T., Hreinnsson E. O. and Woods, R. A.: Representing spatial variability of snow water equivalent in hydrologic and land-surface models: A review, *Water Resour. Res.*, 47, <https://doi.org/10.1029/2011WR010745>, 2011
- Clark, P., Roberts, N., Lean, H., Ballard, S. P., and Charlton-Perez, C.: Convection-permitting models: a step-change in rainfall forecasting. *Meteorol. Appl.*, 23(2), 165-181, <https://doi.org/10.1002/met.1538>, 2016
- 755 Comola, F., Kok, J. F., Gaume, J., Paterna, E., and Lehning, M.: Fragmentation of wind-blown snow crystals. *Geophys. Res. Lett.*, 44, 4195-4203, <https://doi.org/10.1002/2017GL073039>, 2017
- Davies, T. D., Palutikof, J. P., Guo, X., Berkofsky, L., & Halliday, J.: Development and testing of a two-dimensional downslope wind model. *Bound.-Lay. Meteorol.*, 73, 279-297, <https://doi.org/10.1007/BF00711260>, 1995
- 760 Deems, J. S., Painter, T. H., and Finnegan, D. C.: Lidar measurement of snow depth: a review. *J. Glaciol.*, 59, 467-47, <https://doi.org/10.3189/2013JoG12J154>, 2013
- Dozier, J.: Spectral signature of alpine snow cover from the Landsat Thematic Mapper. *Remote Sens. Environ.*, 28, 9-22, [https://doi.org/10.1016/0034-4257\(89\)90101-6](https://doi.org/10.1016/0034-4257(89)90101-6), 1989
- Dozier, J., and Frew, J.: Rapid calculation of terrain parameters for radiation modeling from digital elevation data. *IEEE T. Geosci. Remote*, 28, 963-969, <https://doi.org/10.1109/36.58986>, 1990
- 765 Drusch, M., Bello, U. D., Carlier, S., Colin, O., Fernandez, V., Gascon, F., Hoersch, B., Isola, C., Laberinti, P., Martimort, P., Meygret, A., Spoto, F., Sy, O., Marchese, F., and Bargellini, P.: Sentinel-2: ESA's Optical High-Resolution Mission for GMES Operational Services, *Remote Sens. Environ.*, 120, 25–36, <https://doi.org/10.1016/j.rse.2011.11.026>, 2012.
- Dumont, M., Sirguey, P., Arnaud, Y., and Six, D.: Monitoring spatial and temporal variations of surface albedo on Saint Sorlin Glacier (French Alps) using terrestrial photography, *The Cryosphere*, 5, 759-771, <https://doi.org/10.5194/tc-5-759-2011>, 2011
- 770



- Durand, M., and Margulis, S. A.: Effects of uncertainty magnitude and accuracy on assimilation of multiscale measurements for snowpack characterization. *J. Geophys. Res.: Atmos.*, 113(D2), <https://doi.org/10.1029/2007JD008662>, 2008
- Durand, Y., Guyomarc'h, G., Mérindol, L., and Corripio, J. G.: Improvement of a numerical snow drift model and field validation. *Cold Reg. Sci. Technol.*, 43, 93-103, <https://doi.org/10.1016/j.coldregions.2005.05.008>, 2005
- 775 Earth Resources Observation And Science (EROS) Center: Shuttle Radar Topography Mission (SRTM) Non-Void Filled [Data set]. U.S. Geological Survey. <https://doi.org/10.5066/F7K072R7>, 2017
- Ebert, E., Wilson, L., Weigel, A., Mittermaier, M., Nurmi, P., Gill, P., Gober, M., Joslyn, S., Brown, B., Fowler, T., and Watkins, A.: Progress and challenges in forecast verification. *Meteorol. Appl.*, 20, 130-139, <https://doi.org/10.1002/met.1392>, 2013
- 780 Ellis, C. R., Pomeroy, J. W., Brown, T., and MacDonald, J.: Simulation of snow accumulation and melt in needleleaf forest environments. *Hydrol. Earth Syst. Sc.*, 14, 925-940, <https://doi.org/10.5194/hess-14-925-2010>, 2010
- Essery, R., Li, L., and Pomeroy, J. W.: A distributed model of blowing snow over complex terrain. *Hydrol. Process.*, 13, 2423-2438, [https://doi.org/10.1002/\(SICI\)1099-1085\(199910\)13:14<2423::AID-HYP853>3.0.CO;2-U](https://doi.org/10.1002/(SICI)1099-1085(199910)13:14<2423::AID-HYP853>3.0.CO;2-U), 1999
- Fang, X., Pomeroy, J. W., DeBeer, C. M., Harder, P., and Siemens, E: Hydrometeorological data from Marmot Creek Research Basin, Canadian Rockies. *Earth Syst. Sci. Data*, 11, <https://doi.org/10.5194/essd-2018-117>, 2019
- 785 Fang, X. and Pomeroy, J. W.: Diagnosis of future changes in hydrology for a Canadian Rockies headwater basin, *Hydrol. Earth Syst. Sci.*, 24, 2731–2754, <https://doi.org/10.5194/hess-24-2731-2020>, 2020
- Fiddes, J., and Gruber, S.: TopoSCALE v. 1.0: downscaling gridded climate data in complex terrain. *Geosci. Model Dev.*, 7, 387-405, <https://doi.org/10.5194/gmd-7-387-2014>, 2014
- 790 Forthofer, J. M., Butler, B. W., and Wagenbrenner, N. S.: A comparison of three approaches for simulating fine-scale surface winds in support of wildland fire management. Part I. Model formulation and comparison against measurements. *International J. Wildland Fire*, 23, 969-981, <https://doi.org/10.1071/WF12089>, 2014
- Freudiger, D., Kohn, I., Seibert, J., Stahl, K., and Weiler, M.: Snow redistribution for the hydrological modeling of alpine catchments, *Wires Water*, 4, <https://doi.org/10.1002/wat2.1232>, 2017
- 795 Garen, D. C., and Marks, D.: Spatially distributed energy balance snowmelt modelling in a mountainous river basin: estimation of meteorological inputs and verification of model results. *J. Hydrol.*, 315, 126-153, <https://doi.org/10.1016/j.jhydrol.2005.03.026>, 2005
- Garvelmann, J., Pohl, S., and Weiler, M.: Spatio-temporal controls of snowmelt and runoff generation during rain-on-snow events in a mid-latitude mountain catchment. *Hydrol. Process.*, 29, 3649-3664, <https://doi.org/10.1002/hyp.10460>, 2015
- 800 Gascoïn, S., Lhermitte, S., Kinnard, C., Bortels, K., and Liston, G. E.: Wind effects on snow cover in Pascua-Lama, Dry Andes of Chile, *Adv. Water Resour.*, 55, 25-39, <https://doi.org/10.1016/j.advwatres.2012.11.013>, 2013
- Gascoïn, S., Grizonnet, M., Bouchet, M., Salgues, G., and Hagolle, O.: Theia Snow collection: high-resolution operational snow cover maps from Sentinel-2 and Landsat-8 data. *Earth Syst. Sci. Data*, 11, 493-514, <https://doi.org/10.5194/essd-11-493-2019>, 2019
- 805 Gascoïn, S.: Time series of snow cover area products over the Kananaskis Country [Data set]. Zenodo. <http://doi.org/10.5281/zenodo.3834623>, 2020
- Gauer, P.: Blowing and drifting snow in Alpine terrain: numerical simulation and related field measurements. *Ann. Glaciol.*, 26, 174-178, <https://doi.org/10.3189/1998AoG26-1-174-178>, 1998
- GDAL/OGR contributors: GDAL/OGR Geospatial Data Abstraction software Library. Open Source Geospatial Foundation. 810 URL <https://gdal.org>, 2020

- Gerber, F., Lehning, M., Hoch, S. W., and Mott, R.: A close-ridge small-scale atmospheric flow field and its influence on snow accumulation. *J. Geophys. Res.-Atmos.*, 122, 7737-7754, <https://doi.org/10.1002/2016JD026258>, 2017
- Gerber, F., Mott, R., and Lehning, M.: The importance of near-surface winter precipitation processes in complex alpine terrain. *J. Hydrometeorol.*, 20, 177-196, <https://doi.org/10.1175/JHM-D-18-0055.1>, 2019
- 815 Groot Zwaaftink, C. D., Löwe, H., Mott, R., Bavay, M., and Lehning, M.: Drifting snow sublimation: A high-resolution 3-D model with temperature and moisture feedbacks, *J. Geophys. Res.-Atmos.*, 116, <https://doi.org/10.1029/2011JD015754>, 2011
- Groot Zwaaftink, C. D., Mott, R., and Lehning, M.: Seasonal simulation of drifting snow sublimation in Alpine terrain. *Water Resour. Res.*, 49, 1581-1590, <https://doi.org/10.1002/wrcr.20137>, 2013
- 820 Grünewald, T., Bühler, Y., and Lehning, M.: Elevation dependency of mountain snow depth. *The Cryosphere*, 8, 2381-2394, <https://doi.org/10.5194/tc-8-2381-2014>, 2014
- Hagolle, O., Huc, M., Desjardins, C., Auer, S., and Richter, R.: MAJA Algorithm Theoretical Basis Document, <https://doi.org/10.5281/zenodo.1209633>, 2017
- Hansen, M. C., Potapov, P. V., Moore, R., Hancher, M., Turubanova, S. A. A., Tyukavina, A., ... and Kommareddy, A.: High-resolution global maps of 21st-century forest cover change. *Science*, 342, 850-853, <https://doi.org/10.1126/science.1244693>, 2013
- 825 Hanzer, F., Helfricht, K., Marke, T., and Strasser, U.: Multilevel spatiotemporal validation of snow/ice mass balance and runoff modeling in glacierized catchments. *The Cryosphere*, 10, 1859-1881, <https://doi.org/10.5194/tc-10-1859-2016>, 2016
- Hanzer, F., Förster, K., Nemeč, J., and Strasser, U.: Projected cryospheric and hydrological impacts of 21st century climate change in the Ötztal Alps (Austria) simulated using a physically based approach, *Hydrol. Earth Syst. Sci.*, 22, 1593-1614, <https://doi.org/10.5194/hess-22-1593-2018>, 2018
- 830 Harder, P., and Pomeroy, J. W.: Estimating precipitation phase using a psychrometric energy balance method. *Hydrol. Process.*, 27, 1901-1914, <https://doi.org/10.1002/hyp.9799>, 2013
- Harder, P., Schirmer, M., Pomeroy, J. W., and Helgason, W.: Accuracy of snow depth estimation in mountain and prairie environments by an unmanned aerial vehicle. *The Cryosphere*, 10, 2559-2571, <https://doi.org/10.5194/tc-10-2559-2016>, 2016
- 835 Harder, P., Pomeroy, J. W., & Helgason, W.: Local-scale advection of sensible and latent heat during snowmelt. *Geophys. Res. Lett.*, 44, 9769-9777, <https://doi.org/10.1002/2017GL074394>, 2017
- Havens, S., Marks, D., FitzGerald, K., Masarik, M., Flores, A. N., Kormos, P., and Hedrick, A.: Approximating Input Data to a Snowmelt Model Using Weather Research and Forecasting Model Outputs in Lieu of Meteorological Measurements. *J. Hydrometeorol.*, 20, 847-862, <https://doi.org/10.1175/JHM-D-18-0146.1>, 2019
- 840 He, S., and Ohara, N.: Modeling Subgrid Variability of Snow Depth Using the Fokker-Planck Equation Approach. *Water Resour. Res.*, 55(4), 3137-3155, <https://doi.org/10.1029/2017WR022017>, 2019
- Hedrick, A. R., Marks, D., Havens, S., Robertson, M., Johnson, M., Sandusky, M., Marschall H.-P., Kormos, P. R., Bormann, K. J., and Painter, T. H.: Direct insertion of NASA Airborne Snow Observatory-derived snow depth time series into the iSnobal energy balance snow model. *Water Resour. Res.*, 54, 8045-8063, <https://doi.org/10.1029/2018WR023190>, 2018
- 845 Hedstrom, N. R., and Pomeroy, J. W.: Measurements and modelling of snow interception in the boreal forest. *Hydrol. Process.*, 12(10-11), 1611-1625, [https://doi.org/10.1002/\(SICI\)1099-1085\(199808/09\)12:10/11<1611::AID-HYP684>3.0.CO;2-4](https://doi.org/10.1002/(SICI)1099-1085(199808/09)12:10/11<1611::AID-HYP684>3.0.CO;2-4), 1998
- Helbig, N., and van Herwijnen, A. (2017). Subgrid parameterization for snow depth over mountainous terrain from flat field snow depth. *Water Resour. Res.*, 53, 1444-1456, <https://doi.org/10.1002/2016WR019872>, 2017
- 850 Horvath, K., Koracin, D., Vellore, R., Jiang, J., and Belu, R.: Sub-kilometer dynamical downscaling of near-surface winds in complex terrain using WRF and MM5 mesoscale models, *J. Geophys. Res.-Atmos.*, 117(D11), <https://doi.org/10.1029/2012JD017432>, 2012

- Horton, S., and Jamieson, B.: Modelling hazardous surface hoar layers across western Canada with a coupled weather and snow cover model. *Cold Reg. Sci. Technol.*, 128, 22-31, <https://doi.org/10.1016/j.coldregions.2016.05.002>, 2016
- 855 Houze Jr, R. A.: Orographic effects on precipitating clouds. *Rev. Geophys.*, 50, <https://doi.org/10.1029/2011RG000365>, 2012
- Jarosch, A. H., Anslow, F. S., and Clarke, G. K.: High-resolution precipitation and temperature downscaling for glacier models, *Clim. Dynam.*, 38, 391-409, <https://doi.org/10.1007/s00382-010-0949-1>, 2012
- Kienzle, S. W.: Effects of area under-estimations of sloped mountain terrain on simulated hydrological behaviour: a case study using the ACRU model. *Hydrol. Process.*, 25, 1212-1227, <https://doi.org/10.1002/hyp.7886>, 2011
- 860 Kirchner, P. B., Bales, R. C., Molotch, N. P., Flanagan, J., and Guo, Q.: LiDAR measurement of seasonal snow accumulation along an elevation gradient in the southern Sierra Nevada, California. *Hydrol. Earth Syst. Sci.*, 18, <https://doi.org/10.5194/hess-18-4261-2014>, 2014
- Kunkel, K. E.: Simple procedures for extrapolation of humidity variables in the mountainous western United States, *J. Climate*, 2, 656-669, [https://doi.org/10.1175/1520-0442\(1989\)002<0656:SPFEOH>2.0.CO;2](https://doi.org/10.1175/1520-0442(1989)002<0656:SPFEOH>2.0.CO;2), 1989
- 865 Lapen, D. and Martz, L.: The measurement of two simple topographic indices of wind sheltering-exposure from raster digital elevation models *Comput. Geosci.*, 19, 769-779., [https://doi.org/10.1016/0098-3004\(93\)90049-B](https://doi.org/10.1016/0098-3004(93)90049-B), 1993
- Lapo, K. E., Hinkelman, L. M., Raleigh, M. S., and Lundquist, J. D.: Impact of errors in the downwelling irradiances on simulations of snow water equivalent, snow surface temperature, and the snow energy balance. *Water Resour. Res.*, 51, 1649-1670, <https://doi.org/10.1002/2014WR016259>, 2015
- 870 Lehning, M., Löwe, H., Ryser, M., and Raderschall, N.: Inhomogeneous precipitation distribution and snow transport in steep terrain. *Water Resour. Res.*, 44, <https://doi.org/10.1029/2007WR006545>, 2008
- Li, L., and Pomeroy, J. W.: Estimates of threshold wind speeds for snow transport using meteorological data, *J. Appl. Meteorol.*, 36, 205-213, [https://doi.org/10.1175/1520-0450\(1997\)036<0205:EOTWSF>2.0.CO;2](https://doi.org/10.1175/1520-0450(1997)036<0205:EOTWSF>2.0.CO;2), 1997
- Liston, G. E.: Representing subgrid snow cover heterogeneities in regional and global models. *J. Climate*, 17, 1381-1397, [https://doi.org/10.1175/1520-0442\(2004\)017<1381:RSSCHI>2.0.CO;2](https://doi.org/10.1175/1520-0442(2004)017<1381:RSSCHI>2.0.CO;2), 2004
- 875 Liston, G. E., & Elder, K.: A meteorological distribution system for high-resolution terrestrial modeling (MicroMet). *J. Hydrometeorol.*, 7(2), 217-234, <https://doi.org/10.1175/JHM486.1>, 2006
- Liston, G. E., Hachnel, R. B., Sturm, M., Hiemstra, C. A., Berezovskaya, S., and Tabler, R. D.: Simulating complex snow distributions in windy environments using SnowTran-3D, *J. Glaciol.*, 53, 241-256, <https://doi.org/10.3189/172756507782202865>, 2007
- 880 Luijting, H., Vikhamar-Schuler, D., Aspelien, T., Bakketun, Å., and Homleid, M.: Forcing the SURFEX/Crocus snow model with combined hourly meteorological forecasts and gridded observations in southern Norway. *The Cryosphere*, 12, 2123-2145, <https://doi.org/10.5194/tc-12-2123-2018>, 2018
- Lundquist, J., Hughes, M., Gutmann, E., and Kapnick, S.: Our skill in modeling mountain rain and snow is bypassing the skill of our observational networks. *B. Am. Meteorol. Soc.*, 100, 2473-2490, <https://doi.org/10.1175/BAMS-D-19-0001.1>, 2019.
- 885 Lv, Z., & Pomeroy, J. W.: Assimilating snow observations to snow interception process simulations. *Hydrol. Proc.*, 34, 2229-2246, <https://doi.org/10.1002/hyp.13720>, 2020
- Macander, M. J., Swingley, C. S., Joly, K., and Reynolds, M. K.: Landsat-based snow persistence map for northwest Alaska. *Remote Sens. Environ.*, 163, 23-31, <https://doi.org/10.1016/j.rse.2015.02.028>, 2015
- 890 MacDonald, M. K., Pomeroy, J. W., and Pietroniro, A.: On the importance of sublimation to an alpine snow mass balance in the Canadian Rocky Mountains, *Hydrol. Earth Syst. Sc.*, 14, 1401, <https://doi.org/10.5194/hess-14-1401-2010>, 2010
- Marks, D., and Dozier, J. Climate and energy exchange at the snow surface in the alpine region of the Sierra Nevada: 2. Snow cover energy balance. *Water Resour. Res.*, 28(11), 3043-3054, <https://doi.org/10.1029/92WR01483>, 1992

- 895 Marks, D., Domingo, J., Susong, D., Link, T., and Garen, D.: A spatially distributed energy balance snowmelt model for application in mountain basins, *Hydrol. Process.*, 13, 1935-1959, [https://doi.org/10.1002/\(SICI\)1099-1085\(199909\)13:12/13<1935::AID-HYP868>3.0.CO;2-C](https://doi.org/10.1002/(SICI)1099-1085(199909)13:12/13<1935::AID-HYP868>3.0.CO;2-C), 1999
- Marsh, C. B., Pomeroy, J. W., and Spiteri, R. J.: Implications of mountain shading on calculating energy for snowmelt using unstructured triangular meshes. *Hydrol. Process.*, 26, 1767-1778, <https://doi.org/10.1002/hyp.9329>, 2012
- 900 Marsh, C. B., Spiteri, R. J., Pomeroy, J. W., and Wheeler, H. S.: Multi-objective unstructured triangular mesh generation for use in hydrological and land surface models. *Comput. Geosci.*, 119, 49-67, <https://doi.org/10.1016/j.cageo.2018.06.009>, 2018
- Marsh, C. B., Pomeroy, J. W., Spiteri, R. J., and Wheeler, H. S.: A finite volume blowing snow model for use with variable resolution meshes. *Water Resour. Res.*, 56, <https://doi.org/10.1029/2019WR025307>, 2020a
- 905 Marsh, C. B., Pomeroy, J. W., and Wheeler, H. S.: The Canadian Hydrological Model (CHM) v1.0: a multi-scale, multi-extent, variable-complexity hydrological model—design and overview. *Geosci. Mod. Dev.*, 13, <https://doi.org/10.5194/gmd-13-225-2020>, 2020b
- Marty, C., Philipona, R., Fröhlich, C., and Ohmura, A.: Altitude dependence of surface radiation fluxes and cloud forcing in the Alps: results from the alpine surface radiation budget network. *Theor. Appl. Climatol.*, 72, 137-155, <https://doi.org/10.1007/s007040200019>, 2002
- 910 Menke, R., Vasiljević, N., Mann, J., and Lundquist, J. K.: Characterization of flow recirculation zones at the Perdigão site using multi-lidar measurements, *Atmos. Chem. Phys.*, 19, 2713–2723, <https://doi.org/10.5194/acp-19-2713-2019>, 2019.
- Milbrandt, J. A., Bélair, S., Faucher, M., Vallée, M., Carrera, M. L., and Glazer, A.: The pan-Canadian high resolution (2.5 km) deterministic prediction system. *Weather Forecast.*, 31, 1791-1816, <https://doi.org/10.1175/WAF-D-16-0035.1>, 2016
- 915 Morin, S., Horton, S., Techel, F., Bavay, M., Coléou, C., Fierz, C., Gobiet, A., Hagenmuller, P., Lafaysse, M., Lizar, M., Mitterer, C., Monti, F., Muller, K., Olefs, M., Snook, J. S., van Herwijnen, A., and Vionnet, V.: Application of physical snowpack models in support of operational avalanche hazard forecasting: A status report on current implementations and prospects for the future. *Cold Reg. Sci. Technol.*, 170, 102910, <https://doi.org/10.1016/j.coldregions.2019.102910>, 2020
- Mott, R., and Lehning, M.: Meteorological modeling of very high-resolution wind fields and snow deposition for mountains. *J. Hydrometeorol.*, 11, 934-949, <https://doi.org/10.1175/2010JHM1216.1>, 2010
- 920 Mott, R., Schirmer, M., Bavay, M., Grünewald, T., and Lehning, M.: Understanding snow-transport processes shaping the mountain snow-cover, *The Cryosphere*, 4, 545–559, <https://doi.org/10.5194/tc-4-545-2010>, 2010.
- Mott, R., Gromke, C., Grünewald, T., and Lehning, M.: Relative importance of advective heat transport and boundary layer decoupling in the melt dynamics of a patchy snow cover. *Adv. Water Resour.*, 55, 88-97, <https://doi.org/10.1016/j.advwatres.2012.03.001>, 2013
- 925 Mott, R., Vionnet, V., and Grünewald, T.: The seasonal snow cover dynamics: review on wind-driven coupling processes. *Front. Earth Sci.*, 6, 197, <https://doi.org/10.3389/feart.2018.00197>, 2018
- Mott, R., Wolf, A., Kehl, M., Kunstmann, H., Warscher, M., and Grünewald, T.: Avalanches and micrometeorology driving mass and energy balance of the lowest perennial ice field of the Alps: a case study, *The Cryosphere*, 13, 1247–1265, <https://doi.org/10.5194/tc-13-1247-2019>, 2019.
- 930 Musselman, K. N., Pomeroy, J. W., Essery, R. L., and Leroux, N.: Impact of windflow calculations on simulations of alpine snow accumulation, redistribution and ablation, *Hydrol. Process.*, 29, 3983-3999, <https://doi.org/10.1002/hyp.10595>, 2015
- Naaim-Bouvet, F., Bellot, H., and Naaim, M.: Back analysis of drifting-snow measurements over an instrumented mountainous site. *Ann. Glaciol.*, 51, 207-217, <https://doi.org/10.3189/172756410791386661>, 2010
- Nuth, C., and Kääb, A.: Co-registration and bias corrections of satellite elevation data sets for quantifying glacier thickness change. *The Cryosphere*, 5, 271-290, <https://doi.org/10.5194/tc-5-271-2011>, 2011

- 935 Pelto, B. M., Menounos, B., and Marshall, S. J.: Multi-year evaluation of airborne geodetic surveys to estimate seasonal mass balance, Columbia and Rocky Mountains, Canada. *The Cryosphere*, 13, 1709-1727, <https://doi.org/10.5194/tc-13-1709-2019>, 2019
- Pfeffer, W. T., A. A. Arendt, A. Bliss, T. Bolch, J. G. Cogley, A. S. Gardner, J.-O. Hagen, et al.: The Randolph Glacier Inventory: A Globally Complete Inventory of Glaciers. *J. Glaciol.*, 60, 537–52, <https://doi.org/10.3189/2014JoG13J176>, 2014
- 940 Plüss, C., and Ohmura, A.: Longwave radiation on snow-covered mountainous surfaces. *J. Appl. Meteorol.*, 36, 818-824, <https://doi.org/10.1175/1520-0450-36.6.818>, 1997
- Pomeroy, J. W., and Gray, D. M.: Saltation of snow. *Water Resour. Res.*, 26, 1583-1590, <https://doi.org/10.1029/WR026i007p01583>, 1990
- Pomeroy, J. W., and Male, D. H.: Steady-state suspension of snow, *J. Hydrol.*, 136, 275-301, [https://doi.org/10.1016/0022-1694\(92\)90015-N](https://doi.org/10.1016/0022-1694(92)90015-N), 1992
- 945 Pomeroy, J. W., Gray, D. M., and Landine, P. G.: The prairie blowing snow model: characteristics, validation, operation. *J. Hydrol.*, 144, 165-192, [https://doi.org/10.1016/0022-1694\(93\)90171-5](https://doi.org/10.1016/0022-1694(93)90171-5), 1993
- Pomeroy, J. W., and Gray, D. M.: Snowcover Accumulation, Relocation and Management. National Hydrology Research Institute Science Report No. 7. Environment Canada, Saskatoon, 134 p. 1995. [https://www.usask.ca/hydrology-old/papers/Pomeroy\\_Gray\\_1995.pdf](https://www.usask.ca/hydrology-old/papers/Pomeroy_Gray_1995.pdf)
- 950 Pomeroy, J. W., Gray, D. M., Shook, K. R., Toth, B., Essery, R. L. H., Pietroniro, A., and Hedstrom, N.: An evaluation of snow accumulation and ablation processes for land surface modelling. *Hydrol. Process.*, 12, 2339-2367, [https://doi.org/10.1002/\(SICI\)1099-1085\(199812\)12:15<2339::AID-HYP800>3.0.CO;2-L](https://doi.org/10.1002/(SICI)1099-1085(199812)12:15<2339::AID-HYP800>3.0.CO;2-L), 1998
- Pomeroy, J. W., Gray, D. M., Brown, T., Hedstrom, N. R., Quinton, W. L., Granger, R. J., and Carey, S. K.: The cold regions hydrological model: a platform for basing process representation and model structure on physical evidence. *Hydrol. Process.*, 21, 2650-2667, <https://doi.org/10.1002/hyp.6787>, 2007
- 955 Pomeroy, J. W., Fang, X., and Marks, D. G.: The cold rain-on-snow event of June 2013 in the Canadian Rockies—characteristics and diagnosis. *Hydrol. Process.*, 30, 2899-2914, <https://doi.org/10.1002/hyp.10905>, 2016
- Prein, A. F., Langhans, W., Fosser, G., Ferrone, A., Ban, N., Goergen, K., ... and Brisson, E.: A review on regional convection-permitting climate modeling: Demonstrations, prospects, and challenges. *Rev. Geophys.*, 53, 323-361, <https://doi.org/10.1002/2014RG000475>, 2015
- 960 Pritchard, D. M. W., Forsythe, N., O'Donnell, G., Fowler, H. J., and Rutter, N.: Multi-physics ensemble snow modelling in the western Himalaya, *The Cryosphere*, 14, 1225–1244, <https://doi.org/10.5194/tc-14-1225-2020>, 2020.
- Pudasaini, S. P., and Hutter, K.: *Avalanche dynamics: dynamics of rapid flows of dense granular avalanches*. Springer Science and Business Media, 2007
- 965 Quéno, L., Vionnet, V., Dombrowski-Etchevers, I., Lafaysse, M., Dumont, M., and Karbou, F.: Snowpack modelling in the Pyrenees driven by kilometric-resolution meteorological forecasts. *The Cryosphere*, 10, 1571-1589, <https://doi.org/10.5194/tc-10-1571-2016>, 2016
- 970 Quéno, L., Karbou, F., Vionnet, V., and Dombrowski-Etchevers, I., Satellite products of incoming solar and longwave radiations used for snowpack modelling in mountainous terrain, *Hydrol. Earth Syst. Sci.*, 24, 2083-2104, <https://doi.org/10.5194/hess-24-2083-2020>, 2020
- Raderschall, N., Lehning, M., and Schär, C.: Fine-scale modeling of the boundary layer wind field over steep topography. *Water Resour. Res.*, 44, <https://doi.org/10.1029/2007WR006544>, 2008
- 975 Raleigh, M. S., and Small, E. E.: Snowpack density modeling is the primary source of uncertainty when mapping basin-wide SWE with lidar. *Geophys. Res. Lett.*, 44, 3700-3709, <https://doi.org/10.1002/2016GL071999>, 2017

- Rasouli, K., Pomeroy, J. W., Janowicz, J. R., Carey, S. K., and Williams, T. J.: Hydrological sensitivity of a northern mountain basin to climate change. *Hydrol. Process.*, 28, 4191-4208, <https://doi.org/10.1002/hyp.10244>, 2014
- 980 Rasmussen, R., Liu, C., Ikeda, K., Gochis, D., Yates, D., Chen, F., Tewari, M., Barlage, M., Dudhia, J., Yu, W., Miller, K., Arsenault, K., Grubisic, V., Thompson, G. and Gutmann, E.: High-resolution coupled climate runoff simulations of seasonal snowfall over Colorado: a process study of current and warmer climate. *J. Climate*, 24, 3015-3048, <https://doi.org/10.1175/2010JCLI3985.1>, 2011
- Réveillet, M., MacDonell, S., Gascoïn, S., Kinnard, C., Lhermitte, S., and Schaffer, N.: Impact of forcing on sublimation simulations for a high mountain catchment in the semiarid Andes. *The Cryosphere*, 14, 147-163, <https://doi.org/10.5194/tc-14-147-2020>, 2020
- 985 Ryan, B.: A Mathematical Model for Diagnosis and Prediction of Surface Winds in Mountainous Terrain. *J. Appl. Meteorol.*, 16, 571-584, [https://doi.org/10.1175/1520-0450\(1977\)016<0571:AMMFD>2.0.CO;2](https://doi.org/10.1175/1520-0450(1977)016<0571:AMMFD>2.0.CO;2), 1977
- Rüschendorf, L.: The Wasserstein distance and approximation theorems. *Prob. Theory Rel.*, 70, 117-129, <https://doi.org/10.1007/BF00532240>, 1985
- 990 Sauter, T., Möller, M., Finkelnburg, R., Grabiec, M., Scherer, D., and Schneider, C.: Snowdrift modelling for the Vestfonna ice cap, north-eastern Svalbard, *The Cryosphere*, 7, 1287-1301, <https://doi.org/10.5194/tc-7-1287-2013>, 2013.
- Sexstone, G. A., Clow, D. W., Fassnacht, S. R., Liston, G. E., Hiemstra, C. A., Knowles, J. F., and Penn, C. A.: Snow sublimation in mountain environments and its sensitivity to forest disturbance and climate warming. *Water Resour. Res.*, 54, 1191-1211, <https://doi.org/10.1002/2017WR021172>, 2018
- 995 Schirmer, M., and Pomeroy, J. W.: Processes governing snow ablation in alpine terrain—detailed measurements from the Canadian Rockies. *Hydrol. Earth Syst. Sc.*, 24, 143-157, <https://doi.org/10.5194/hess-24-143-2020>, 2020
- Schlögl, S., Lehning, M., Fierz, C., and Mott, R.: Representation of horizontal transport processes in snowmelt modeling by applying a footprint approach. *Front. Earth Sci.*, 6, <https://doi.org/10.3389/feart.2018.00120>, 2018
- Schneiderbauer, S., and Prokop, A.: The atmospheric snow-transport model: SnowDrift3D. *J. Glaciol.*, 57, 526-542, <https://doi.org/10.3189/002214311796905677>, 2011
- 1000 Shea, J. M., Marshall, S. J., and Livingston, J. M.: Glacier distributions and climate in the Canadian Rockies. *Arct., Antarct., Alp. Res.*, 36, 272-279, [https://doi.org/10.1657/1523-0430\(2004\)036\[0272:GDACIT\]2.0.CO;2](https://doi.org/10.1657/1523-0430(2004)036[0272:GDACIT]2.0.CO;2), 2004
- Slater, A. G., Lawrence, D. M., and Koven, C. D.: Process-level model evaluation: a snow and heat transfer metric, *The Cryosphere*, 11, 989-996, <https://doi.org/10.5194/tc-11-989-2017>, 2017
- 1005 Smith, C. D.: Correcting the wind bias in snowfall measurements made with a Geonor T-200B precipitation gauge and alter wind shield. *Proceedings of the 87<sup>th</sup> American Meteorology Society Annual Meeting*, San Antonio, Texas, 2007
- Sommer, C. G., Lehning, M., and Mott, R.: Snow in a very steep rock face: Accumulation and redistribution during and after a snowfall event. *Front. Earth Sci.*, 3, 73, <https://doi.org/10.3389/feart.2015.00073>, 2015
- Vernay, M., Lafaysse, M., Mérindol, L., Giraud, G., and Morin, S.: Ensemble forecasting of snowpack conditions and avalanche hazard. *Cold Reg. Sci. Technol.*, 120, 251-262, <https://doi.org/10.1016/j.coldregions.2015.04.010>, 2015
- 1010 Versegny, D. L., McFarlane, N. A. and Lazare, M.: Class—A Canadian land surface scheme for GCMS, II. Vegetation model and coupled runs, *Int. J. Climatol.*, 13, 347-370, doi:10.1002/joc.3370130402, <https://doi.org/10.1002/joc.3370130402>, 1993.
- Vionnet, V.: Etudes du transport de la neige par le vent en conditions alpines: observations et simulation à l'aide d'un modèle couplé atmosphère/manteau neigeux, Ph.D. thesis, Sciences et Techniques de l'Environnement, Université Paris-Est, France, <http://tel.archives-ouvertes.fr/tel-00781279>, 2012.
- 1015 Vionnet, V., Guyomarc'h, G., Bouvet, F. N., Martin, E., Durand, Y., Bellot, H., Bel C., and Puglièse, P.: Occurrence of blowing snow events at an alpine site over a 10-year period: observations and modelling, *Adv. Water Resour.*, 55, 53-63, <https://doi.org/10.1016/j.advwatres.2012.05.004>, 2013

- 1020 Vionnet, V., Martin, E., Masson, V., Guyomarc'h, G., Naaim-Bouvet, F., Prokop, A., Durand Y., and Lac, C.: Simulation of wind-induced snow transport and sublimation in alpine terrain using a fully coupled snowpack/atmosphere model. *The Cryosphere*, 8, 395-415, <https://doi.org/10.5194/tc-8-395-2014>, 2014
- Vionnet, V., Bélair, S., Girard, C., and Plante, A.: Wintertime subkilometer numerical forecasts of near-surface variables in the Canadian Rocky Mountains. *Mon. Weather Rev.*, 143, 666-686, <https://doi.org/10.1175/MWR-D-14-00128.1>, 2015
- 1025 Vionnet, V., Dombrowski-Etchevers, I., Lafaysse, M., Quéno, L., Seity, Y., and Bazile, E.: Numerical weather forecasts at kilometer scale in the French Alps: evaluation and application for snowpack modeling. *J. Hydrometeorol.*, 17, 2591-2614, <https://doi.org/10.1175/JHM-D-15-0241.1>, 2016
- Vionnet, V., Martin, E., Masson, V., Lac, C., Bouvet, F. N., and Guyomarc'h, G.: High-Resolution Large Eddy Simulation of Snow Accumulation in Alpine Terrain, *J. Geophys. Res.-Atmos.*, 122, 11-005, <https://doi.org/10.1002/2017JD026947>, 2017
- 1030 Vionnet, V., Six, D., Auger, L., Dumont, M., Lafaysse, M., Quéno, L., Réveillet M., Dombrowski-Etchevers, I, Thibert E., and Vincent, C.: Sub-kilometer precipitation datasets for snowpack and glacier modeling in alpine terrain. *Front. Earth Sci.*, 7, <https://doi.org/10.3389/feart.2019.00182>, 2019
- Wagenbrenner, N. S., Forthofer, J. M., Lamb, B. K., Shannon, K. S., and Butler, B. W.: Downscaling surface wind predictions from numerical weather prediction models in complex terrain with WindNinja. *Atmos. Chem. Phys.*, 16, 5229-5241, <https://doi.org/10.5194/acp-16-5229-2016>, 2016
- 1035 Wagenbrenner, N. S., Forthofer, J. M., Page, W. G., and Butler, B. W.: Development and Evaluation of a Reynolds-Averaged Navier–Stokes Solver in WindNinja for Operational Wildland Fire Applications. *Atmosphere*, 10, 672, <https://doi.org/10.3390/atmos10110672>, 2019
- Walmsley, J. L., Salmon, J. R., and Taylor, P. A.: On the application of a model of boundary-layer flow over low hills to real terrain. *Bound.-Lay. Meteorol.*, 23(1), 17-46, <https://doi.org/10.1007/BF00116110>, 1982
- 1040 Warscher, M., Strasser, U., Kraller, G., Marke, T., Franz, H., and Kunstmann, H.: Performance of complex snow cover descriptions in a distributed hydrological model system: A case study for the high Alpine terrain of the Berchtesgaden Alps. *Water Resour. Res.*, 49, 2619-2637, <https://doi.org/10.1002/wrcr.20219>, 2013
- Wayand, N. E., Marsh, C. B., Shea, J. M., and Pomeroy, J. W.: Globally scalable alpine snow metrics. *Remote Sens. Environ.*, 213, 61-72, <https://doi.org/10.1016/j.rse.2018.05.012>, 2018
- 1045 Winstral, A., and Marks, D.: Simulating wind fields and snow redistribution using terrain-based parameters to model snow accumulation and melt over a semi-arid mountain catchment. *Hydrol. Process.*, 16, 3585-3603, <https://doi.org/10.1002/hyp.1238>, 2002
- Winstral, A., Marks, D., and Gurney, R.: An efficient method for distributing wind speeds over heterogeneous terrain. *Hydrol. Process.*, 23, 2526-2535, <https://doi.org/10.1002/hyp.7141>, 2009
- 1050 Winstral, A., and Marks, D.: Long-term snow distribution observations in a mountain catchment: Assessing variability, time stability, and the representativeness of an index sitem *Water Resour. Res.*, 50, 293-305, <https://doi.org/10.1002/2012WR013038>, 2014
- Winstral, A., Jonas, T., and Helbig, N.: Statistical downscaling of gridded wind speed data using local topography. *J. Hydrometeorol.*, 18, 335-348, <https://doi.org/10.1175/JHM-D-16-0054.1>, 2017
- 1055 Wood, N.: The onset of separation in neutral, turbulent flow over hills. *Bound.-Lay. Meteorol.*, 76, 137-164, <https://doi.org/10.1007/BF00710894>, 1995





1060 **Table 1: Characteristics of the mesh used in this study. The vertical error corresponds the root mean square error to the underlying reference topographic raster.**

Name of the mesh	Minimum triangle area (m <sup>2</sup> )	Maximum triangle area (m <sup>2</sup> )	Median triangle area (m <sup>2</sup> )	Vertical error (m)	Number of triangles
<i>M<sup>15</sup><sub>50</sub></i>	50 × 50	250 × 250	63 × 63	15	101 700

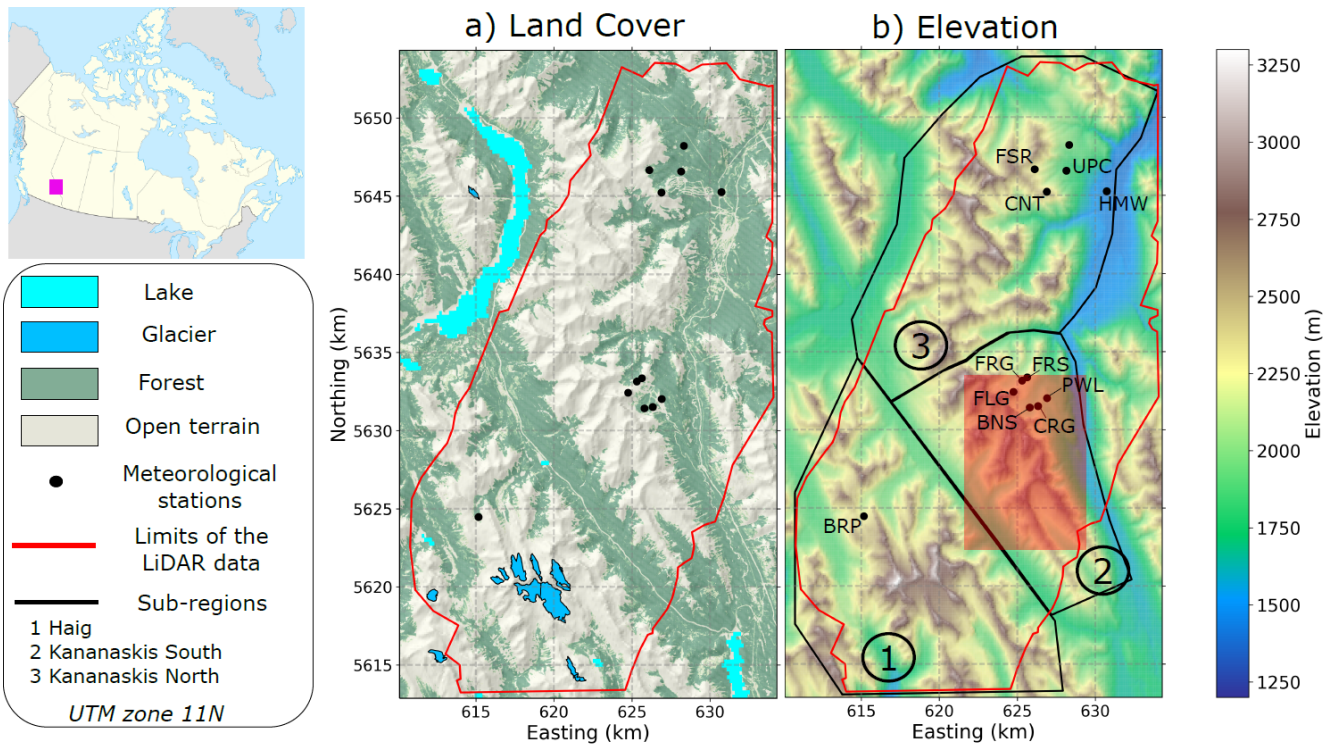
1065 **Table 2: CHM simulations (experiments) used in this study. *Rc* indicates CHM simulations using wind fields from the downscaling method accounting for wind speed reduction in leeward areas. HRDPS refers to the High Resolution Deterministic Prediction System and WN to Wind Ninja. See text for more details.**

Name	Driving Wind Field	Gravitational redistribution	Wind-induced snow transport
<i>NoDown</i>	HRDPS	No	No
<i>NoWndTr NoAv</i>	HRDPS + WN + Rc	No	No
<i>NoWndTr Av</i>	HRDPS + WN + Rc	Yes	No
<i>WndTr Av NoRc</i>	HRDPS + WN	Yes	Yes
<i>WndTr Av Rc</i>	HRDPS + WN+ Rc	Yes	Yes

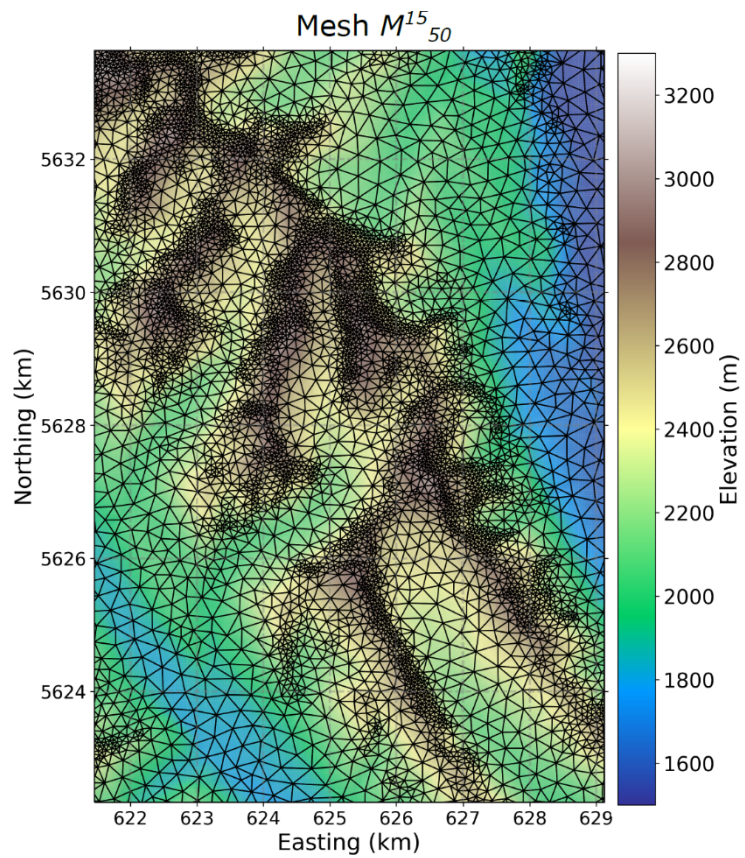
**Table 3: Meteorological stations used for wind evaluation. TPI refers to the Topographic Position Index and is defined as the difference between the elevation of the station minus the mean elevation within a 2-km radius from this station. The location of the stations is shown on Fig. 1.**

Full Name	Code	Latitude (°)	Longitude (°)	Elevation (m)	TPI (m)
Centennial Ridge	CNT	50.9447	-115.937	2470	248
Fisera Ridge	FSR	50.9568	-115.2044	2325	-10
Hay Meadow	HMW	50.9441	-115.1389	1492	-33
Fortress Ledge	FLG	50.8300	-115.2285	2565	216
Fortress Ridge	FRG	50.8364	-115.2209	2327	99
Fortress Ridge South	FRS	50.8382	-115.2158	2306	129
Canadian Ridge	CRG	50.8215	-115.2063	2211	68
Burtsall Pass	BRP	50.7606	-115.3671	2260	-90

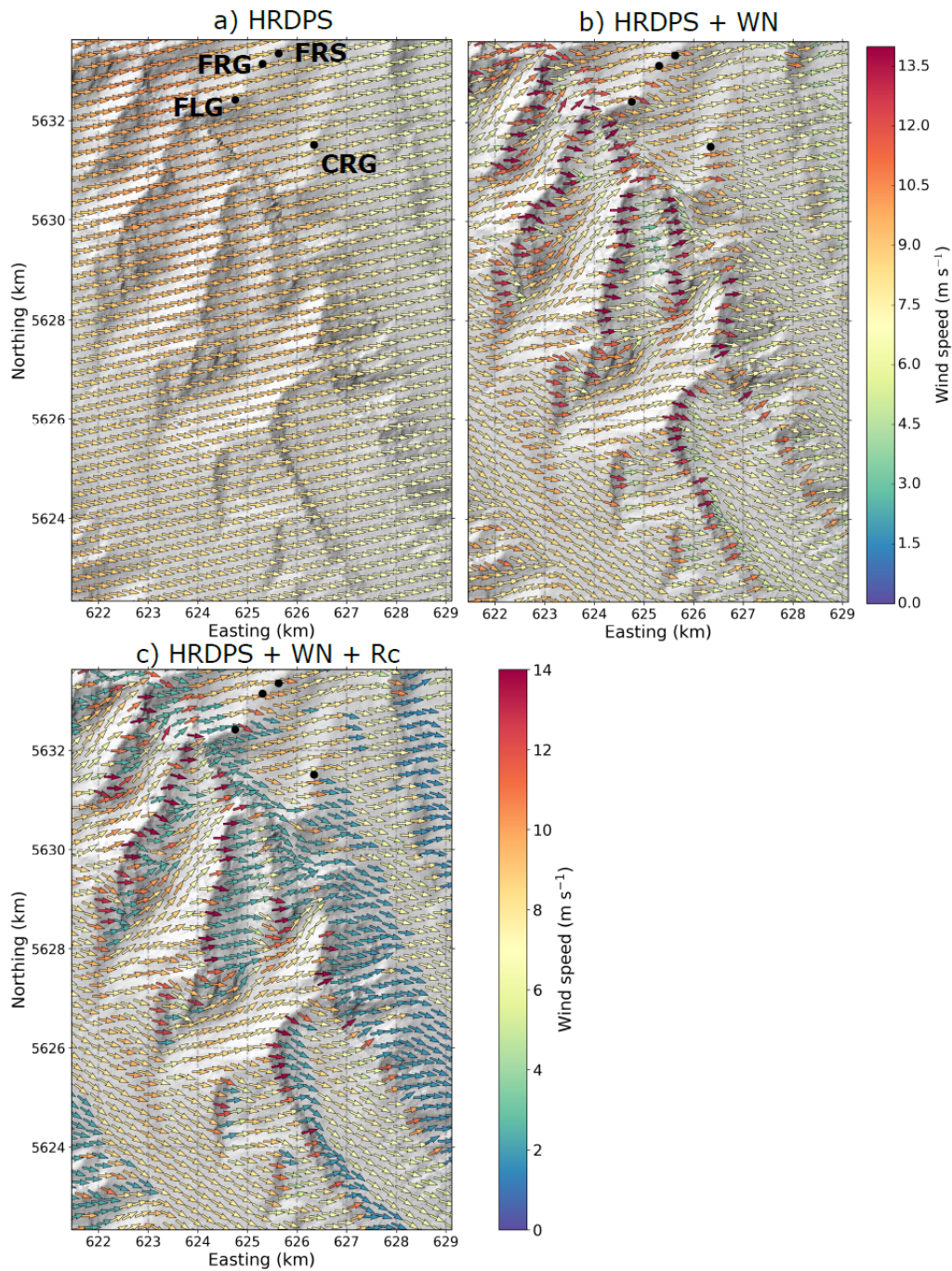
1070



1075 **Figure 1: a) Land cover map and b) elevation map of the Kananaskis Valley, Alberta, Canada study domain. The glacier mask is taken from the Randolph Glacier Inventory version 6.0 (Pfeffer et al., 2014). The red-shaded area correspond to the area shown in Fig. 2, 3 6 and 10. The characteristics of the meteorological stations are given in Tab. 3. Areas labelled from 1 to 3 correspond to sub-regions used in the analysis of the results (see Sect. 2.3.2).**

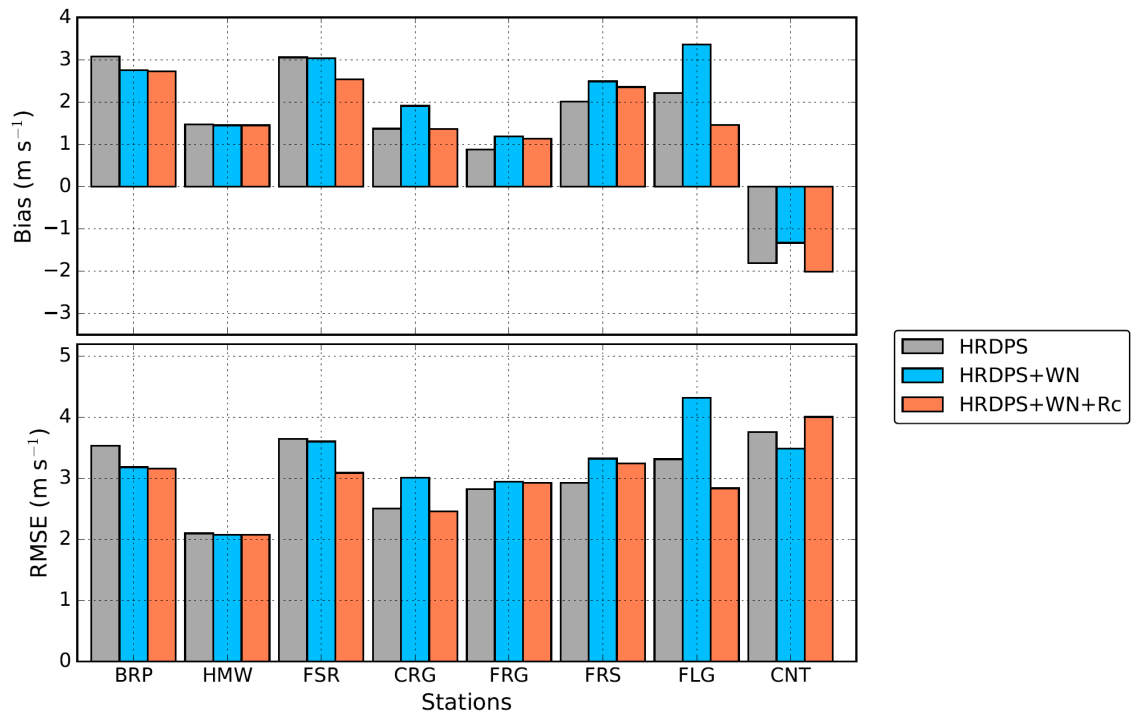


1080 **Figure 2: Variable resolution triangular mesh used in this study over a sub-area of the Kananaskis domain. The location of this sub-area corresponds to the red-shaded area shown on Fig. 1b. The underline DEM was taken from the SRTM mission at 1 arc second.**

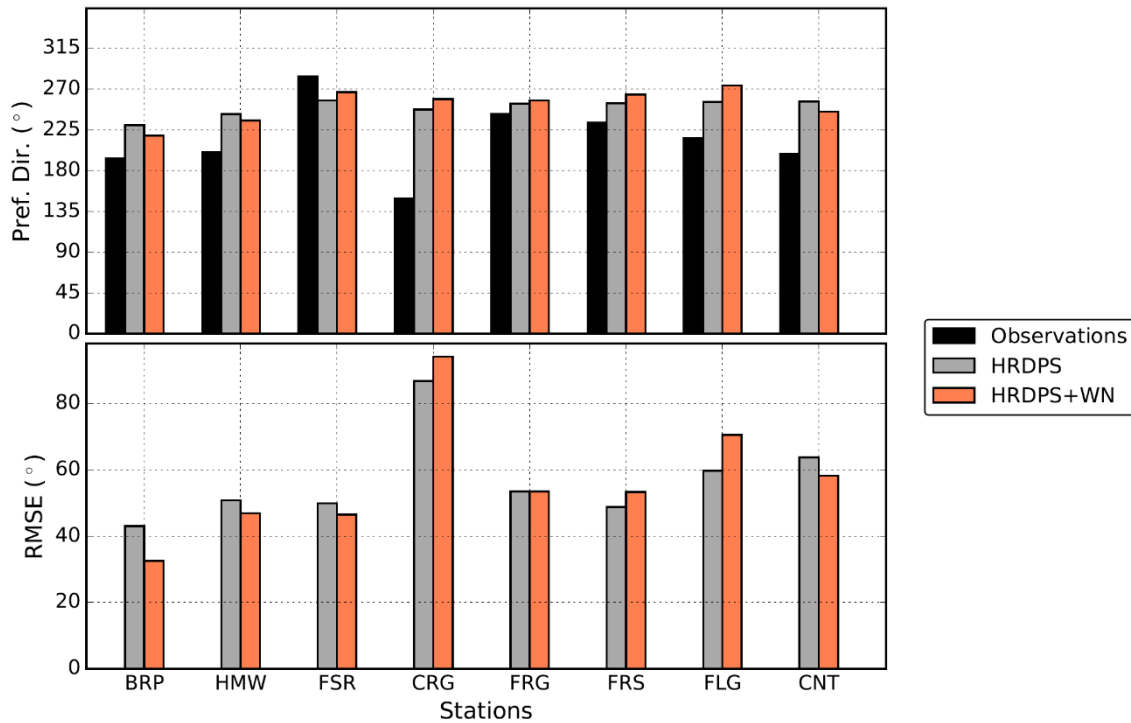


1085

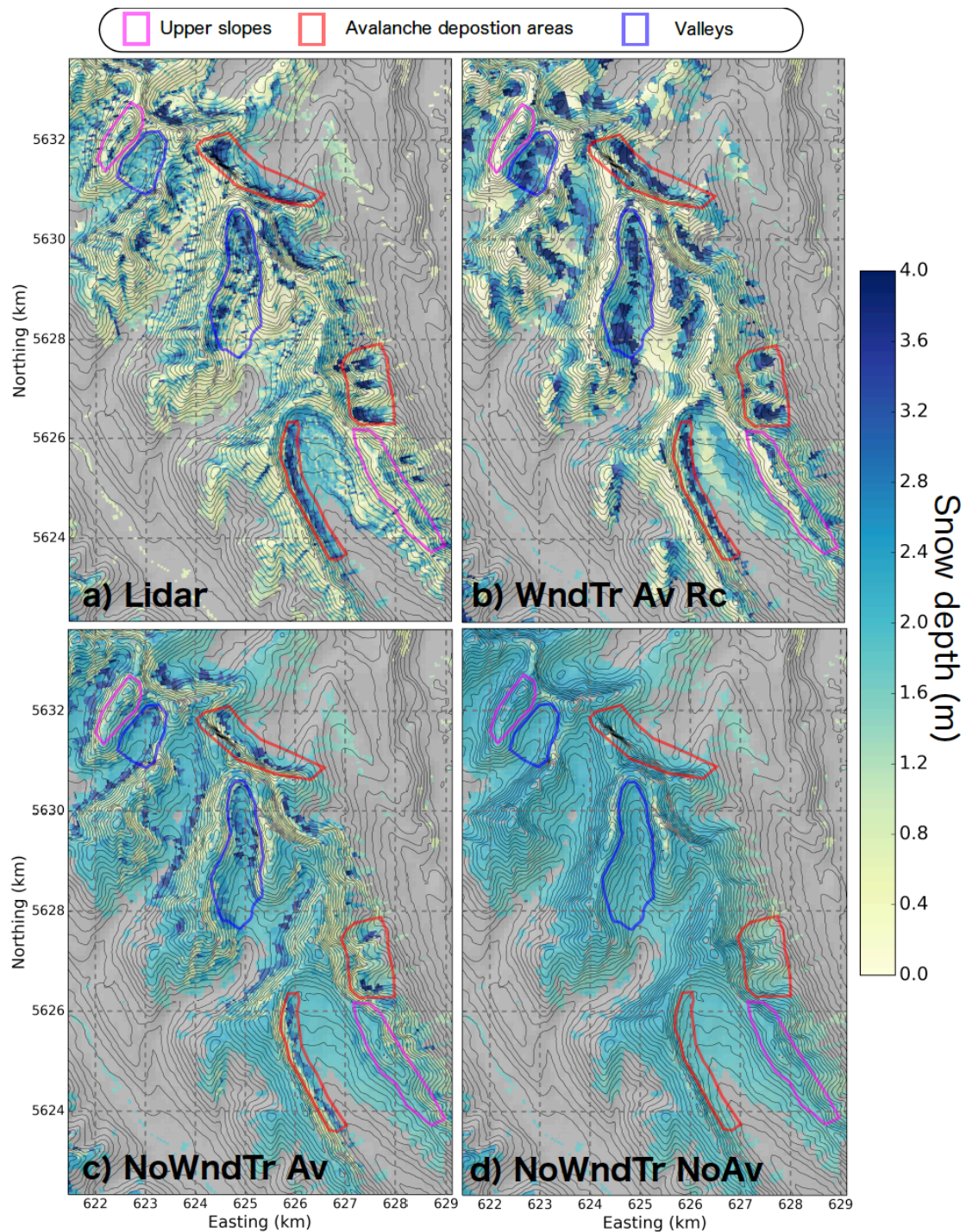
Figure 3: Near-surface wind field on 10 September 2017 at 18 UTC from (a) HRDPS without downscaling, (b) HRDPS downscaled to the CHM mesh  $M^{l^5}_{50}$  using WindNinja and (c) same as (b) but including a parameterization for the formation of recirculation zones on leeward slopes (see Sect. 2.2.4 for more details). The location of this sub-area corresponds to the red-shaded area shown on Fig. 1b. Arrows indicate wind direction while colours indicate wind speed. One arrow is shown every 250 m for clarity. The underlying topography is shown using hill shading. Effects of vegetation on the simulated wind fields are not shown in these maps.



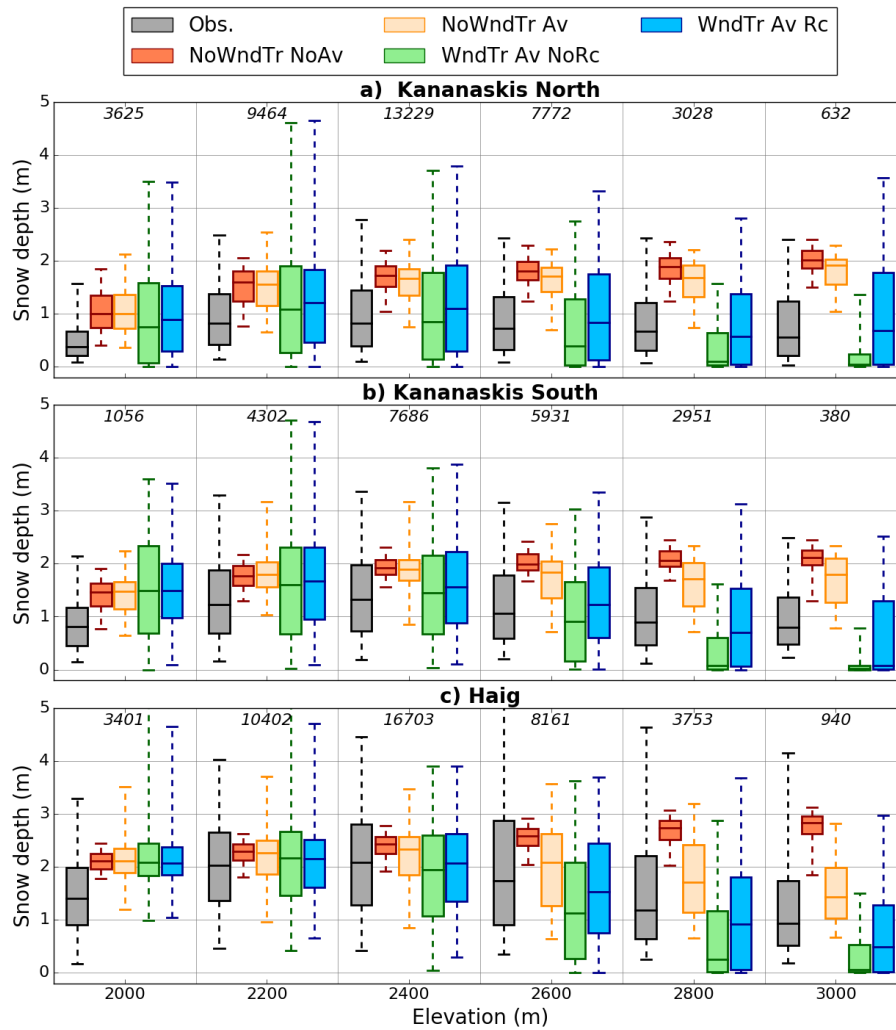
1090 **Figure 4: Evaluation of simulated wind speed using different downscaling methods: (Top) Bias and (Bottom) Root Mean Square Error (RMSE).** Grey colours show the HRDPS wind speed without downscaling, blue colours show the HRDPS wind speed combined with WindNinja microscale winds (HRDPS+WN) and red colours show the same configuration as HRDPS+WN including in addition the wind speed reduction on leeward slopes. Stations used for evaluation are classified by increasing TPI (Table 3). Their location is shown on Fig. 1.



1095 **Figure 5: Same as Fig. 4 for wind direction: (Top) Preferential wind direction and (Bottom) Root Mean Square Error (RMSE). Error metrics were computed for wind direction only when observed wind speed was larger than  $3 \text{ m s}^{-1}$ . Configuration HRDPS+WN+Rc is not shown since the wind direction is unchanged compared to HRDPS+WN.**



1100 **Figure 6:** Snow depth on 27 April 2018 (a) measured by ALS and simulated by three CHM configurations: (b) *WndTr Av Rc*, (c) *NoWndTr Av*, and (d) *NoWndTr NoAv* (Table 3). Properties of snow depth distribution in areas with coloured contours are discussed in the text. Pixels covered by tall vegetation in the observations and in the simulations are excluded from the comparison and appear in grey. Black isolines correspond to  $\Delta z = 50$  m and the location of this region is shown on Fig. 1b.



1105 **Figure 7: Boxplots showing the distributions of observed and simulated snow depth per 200-m elevation bands for three sub-regions. The location of these sub-regions is shown on Fig. 1b. Results of four CHM experiments are shown. The numbers in italic indicate the number of grid points within each elevation band. The whiskers show the 5<sup>th</sup> and 95<sup>th</sup> percentiles and outliers are not plotted.**



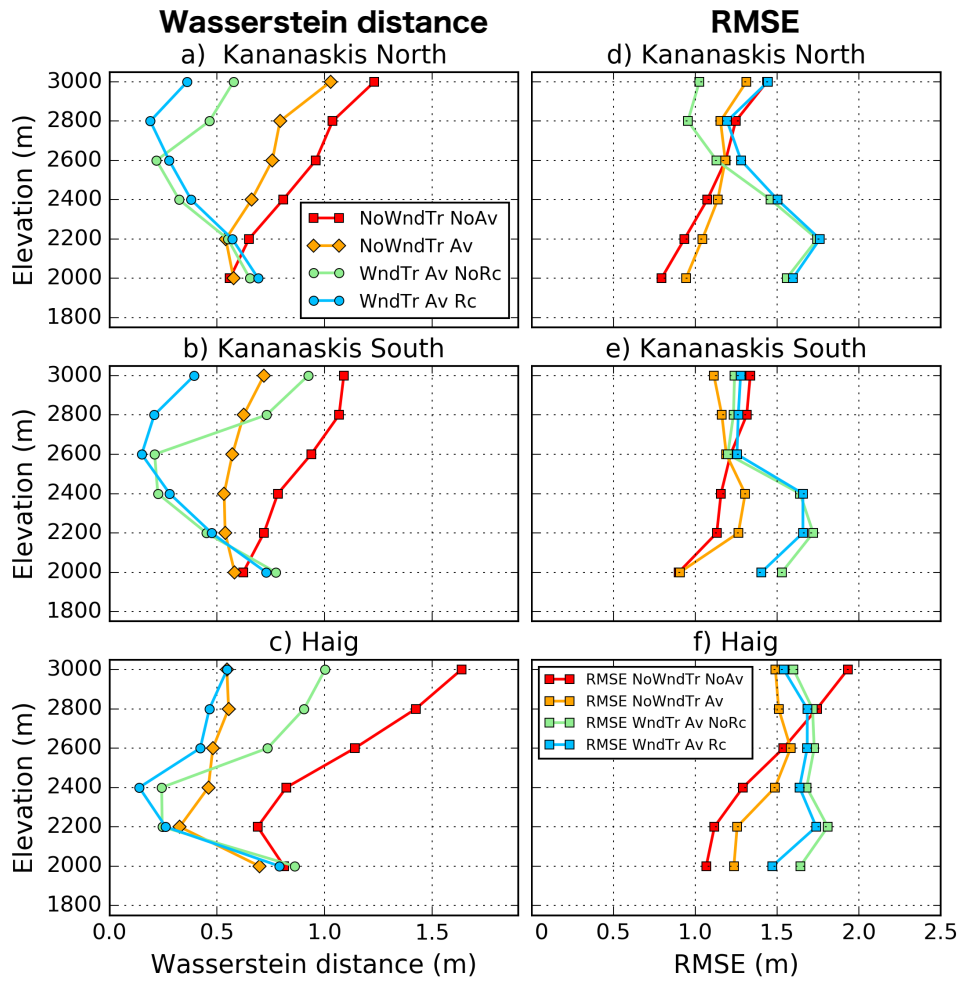
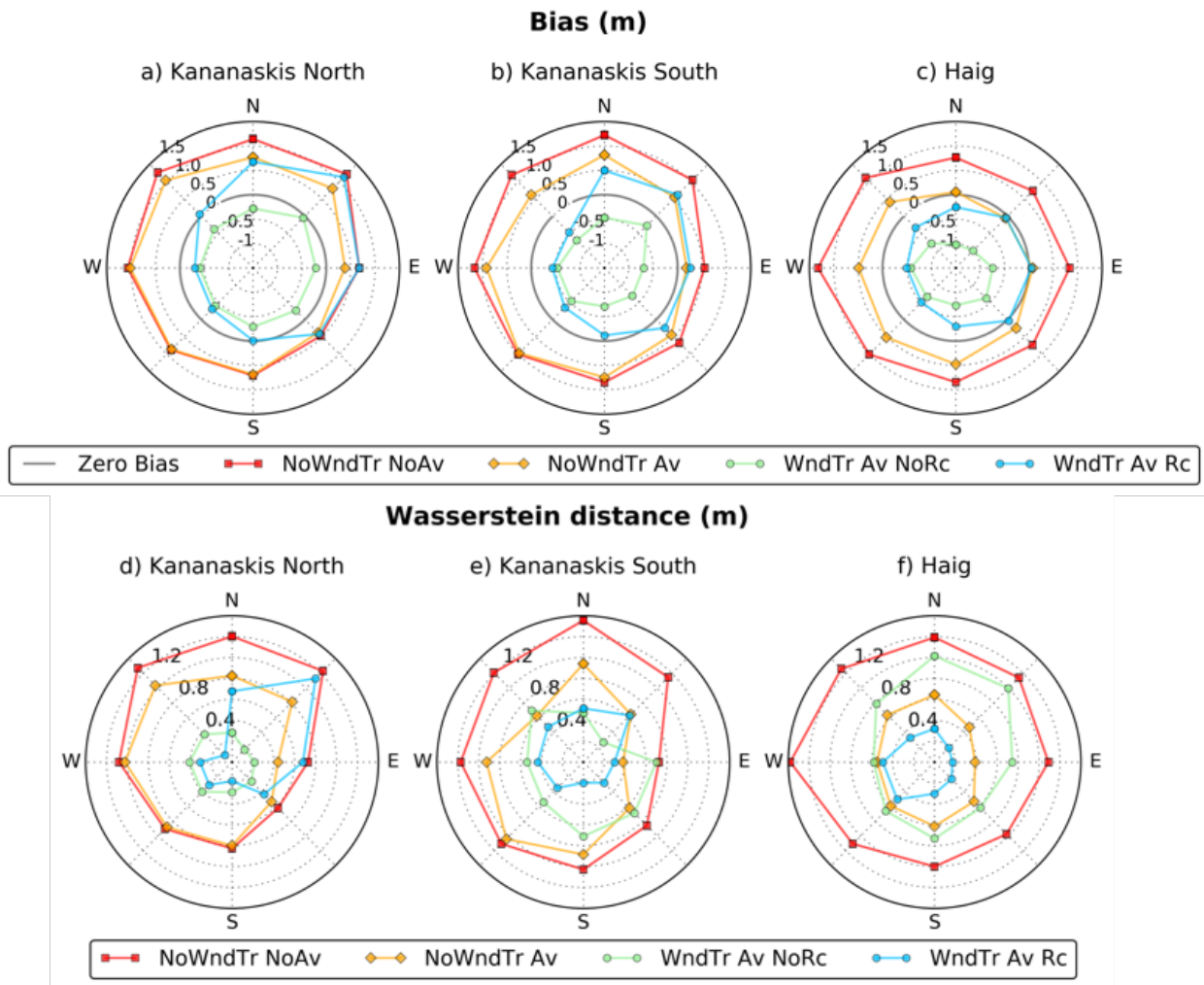
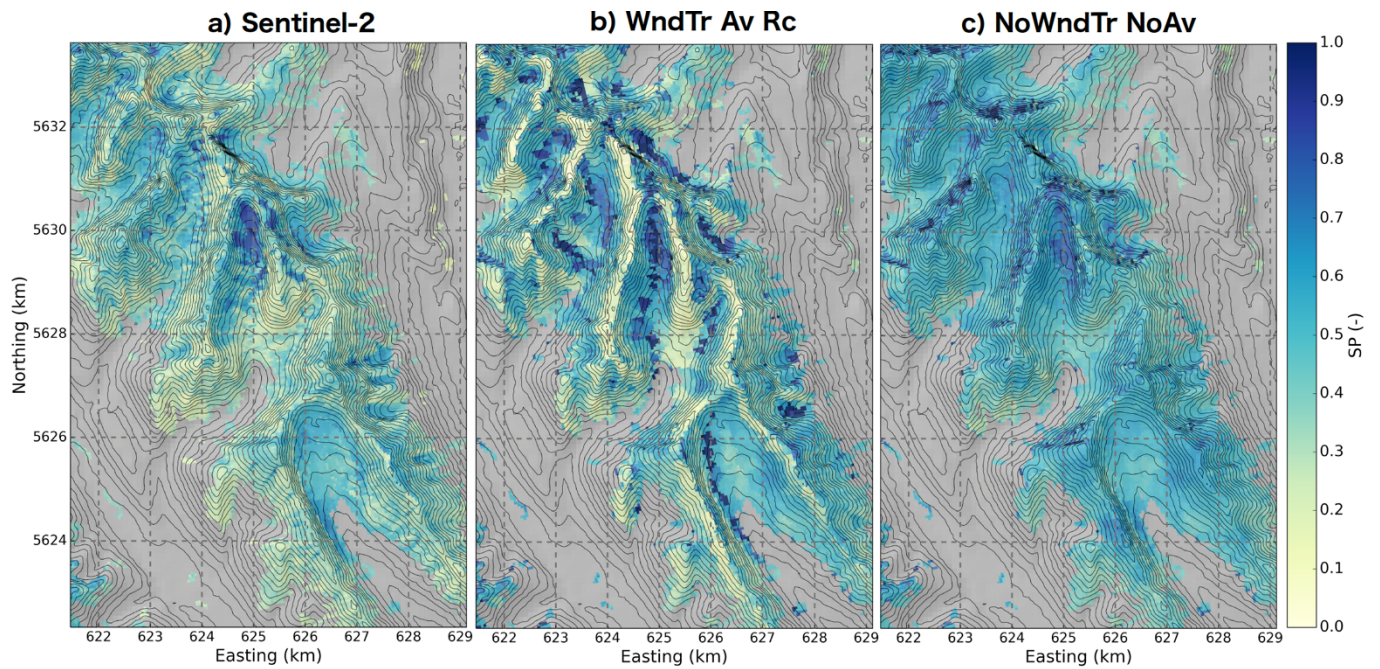


Figure 8: Wasserstein distance and RMSE between observed and simulated snow depth distribution as a function of elevation for four CHM experiments and three sub-regions. The location of these sub-regions is shown on Fig. 1.



1110

Figure 9: Bias (Top) and Wasserstein distance (Bottom) between observed and simulated snow depth distribution in upper slopes as a function of slope orientation for four CHM experiments and three sub-regions. The location of these sub-regions is shown on Fig. 1. Upper slopes are defined as regions of TPI larger than 150 m (see Sect. 2.3.2). The thick grey circles on graphs a, b and c indicate a zero bias. Values outside this circle indicate a positive bias whereas values within this circle indicate a negative bias.



115

**Figure 10: Maps of snow persistence index (SP) (a) derived from Sentinel-2 and simulated by two CHM configurations: (b) *WndTr Av Rc*, and (c) *NoWndTr NoAv* (Table 3). Pixels covered by tall vegetation in the observations and in the simulations are excluded from the comparison and appear in grey. Black isolines correspond to  $\Delta z = 50$  m and the location of this region is shown on Fig. 1b.**

120

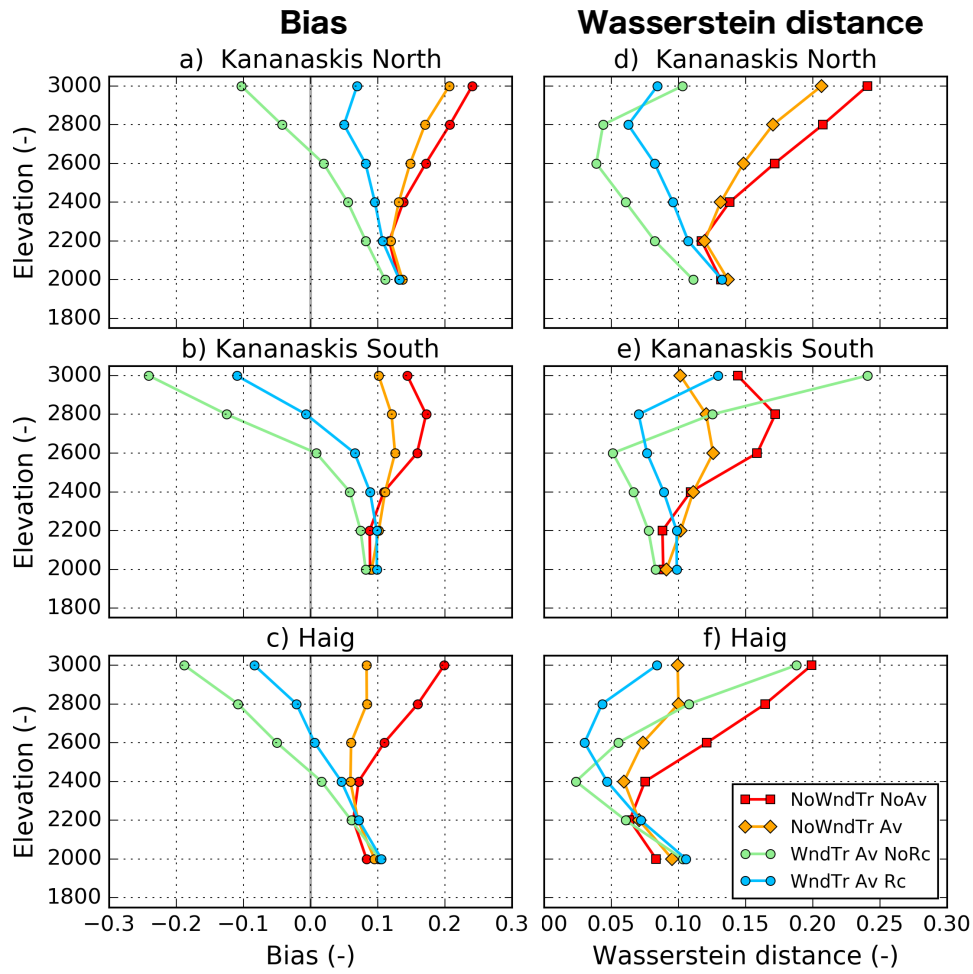
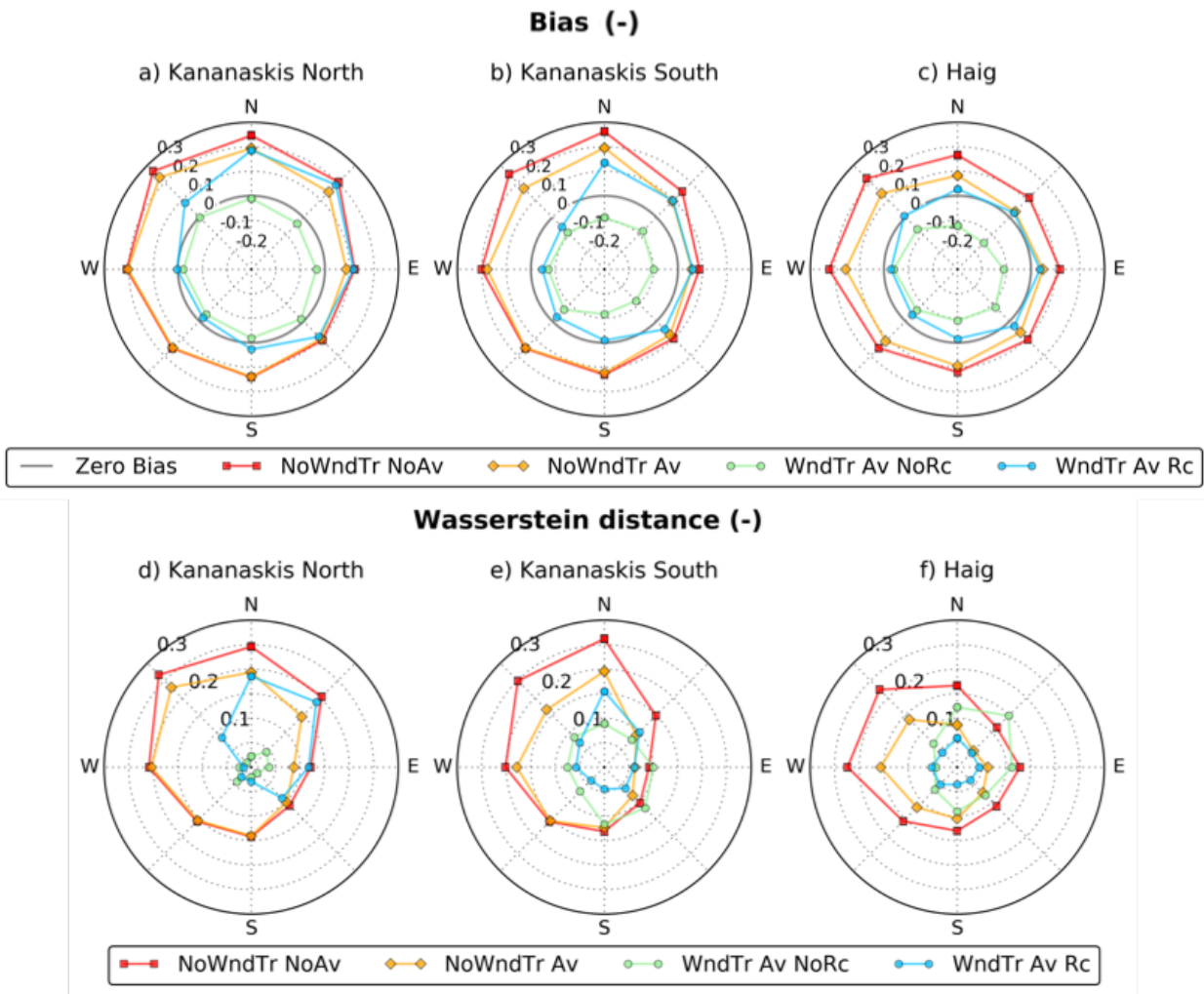


Figure 11: Bias and Wasserstein distance between observed and simulated snow persistence index as a function of elevation for four CHM experiments and three sub-regions. The location of these sub-regions is shown on Fig. 1.



1125 Figure 12: Same as Fig. 9 for the snow persistence index (SP)